sustainability

MDPI

Article

Recycled PET as a Modular System for Coastal Slope Stabilisation: A Preliminary Numerical Climate-Adaptation Approach in Chucuito, Callao

Tito Roberto Vilchez Vilchez [1], Oswaldo Velásquez Hidalgo [2], Maria Cecilia Chirinos Flores [2,*], Guisela Yabar Torres [2], Manuel Félix Villena Mávila [2], Dan Nelson Herrera Ayoque [3], Adler Deker Machado Huanca [1], Hans Aarón Vilchez Chumpitaz [4] and Juan Carlos Gomez Avalos [5]

1 Faculty of Mechanical Engineering, National University of Engineering (UNI), Lima 15333, Peru; tvilchez@uni.edu.pe (T.R.V.V.); amachadoh@uni.edu.pe (A.D.M.H.)
2 Faculty of Architecture and Urbanism, Universidad Ricardo Palma (URP), Lima 15039, Peru; ovelasquez@urp.edu.pe (O.V.H.); guisela.yabar@urp.edu.pe (G.Y.T.); manuel.villena@urp.edu.pe (M.F.V.M.)
3 Environmental Evaluation and Enforcement Agency (OEFA), Lima 15076, Peru; deam07@oefa.gob.pe
4 Faculty of Civil Engineering, Peruvian University of Applied Sciences (UPC), Lima 15023, Peru; pcchivil@upc.edu.pe
5 Directorate of Solid Earth Sciences, Instituto Geofísico del Perú (IGP), Lima 15494, Peru; jgomez@igp.gob.pe
* Correspondence: maria.chirinos@urp.edu.pe; Tel.: +51-982-245-142

Abstract

Vulnerable coastal urban margins face overlapping pressures from erosion, climate change, and plastic-waste accumulation. This study presents a screening-level numerical assessment of a hollow modular unit made of a recycled polyethylene terephthalate (PET)–concrete composite, proposed for coastal slope protection and stabilisation in Chucuito, Callao, Peru. A limit-equilibrium baseline indicates that the unprotected slope is marginal to unstable under the site's seismic demand, motivating the evaluation of a surface-protection concept through a parallel, one-way finite element analysis–computational fluid dynamics (FEA–CFD) framework applied at three slope angles (60°, 53°, 45°). The FEA structural-response screening indicates consistent trends across configurations under an equivalent impact load and the adopted basal restraint. For the hydraulic comparison, inlet velocities of 3, 5 and 7 m/s were anchored to the site-specific Delft3D inundation modelling (site maximum 5 m/s), with a conservative 10 m/s upper bound; relative to a rip-rap reference, the hollow configuration suggests midpoint run-up velocity reductions of approximately 52% at $\theta = 53°$ under the conservative scenario and ≈57% at 3 and 5 m/s, falling to ≈25% at 7 m/s with overlapping ranges and the simulated free surface exceeding the crest. The CFD free-surface elevations show order-of-magnitude consistency with an indicative EurOtop-based run-up benchmark used as a consistency check rather than as hydraulic validation. Independent of this hydraulic comparison, the hollow geometry saves ≈ 62% of the material volume relative to an equivalent solid concrete block, valorises ≈ 793 post-consumer PET bottles per unit at a 10% dosage, and suggests a 42–58% embodied-CO_2 reduction relative to the same solid-concrete reference, driven mainly by the hollow geometry rather than by the PET substitution itself. The results are internally consistent but not experimentally validated and are intended as a comparative baseline to guide subsequent experimental and field studies, in line with Sustainable Development Goals (SDG) 11, 12 and 13.

Keywords: recycled PET; coastal slope stabilisation; modular unit; finite element analysis; circular economy; climate adaptation; Callao

Check for updates

Academic Editors: Sanjay Nimbalkar and Ivan Sakhno

Received: 30 May 2026
Revised: 24 July 2026
Accepted: 24 July 2026
Published: 11 August 2026

1. Introduction

Coastal areas concentrate environmental, territorial, and material pressures that are often addressed in a fragmented manner. Recent assessments and global data sources indicate that erosion, flooding, and ground destabilisation in shoreline regions are intensified by climate change, anthropogenic pressure, and infrastructure expansion [1–4]. Compound risks from extremes and combined drivers, such as storms, energetic waves, and morphodynamic changes, further challenge mean-trend approaches [1,2]. Consequently, the literature on coastal resilience converges on the need for multi-scale, sustainability-oriented adaptation criteria rather than point-based responses [1,2]. In parallel, the global plastics-production and waste-management system faces a structural crisis. Reports from the Organisation for Economic Co-operation and Development and complementary global assessments agree that global plastic production continues to grow while only a limited fraction effectively returns to productive cycles [3,5]. As a result, a significant proportion of these materials accumulates in landfills, is incinerated, or is dispersed in terrestrial and marine environments [3,5]. Studies on plastic pollution, circular economy, and waste management warn that this phenomenon should not be understood solely as a final-disposal problem, but as a systemic failure linked to linear economies, low material circularity, and limited absorption capacity of management systems [5–7]. This issue is particularly relevant in coastal territories, where plastic waste converges with fragile ecosystems, complex hydrometeorological dynamics, and a high density of human activities. In Peru, official data from the Ministry of the Environment show a particularly concentrated territorial expression in Metropolitan Lima and Callao, where a significant proportion of the country's plastic waste is generated [6]. This coincidence between waste-related environmental pressure and coastal exposure reinforces the relevance of exploring material-valorisation routes for streams such as PET, particularly in applications capable of immobilising waste over long periods and reducing demand for virgin materials [6,8]. Within this scenario, PET stands out due to its high presence in post-consumer streams and its potential reincorporation into longer-lifespan applications.

Among different plastic wastes, polyethylene terephthalate (PET) is notable for its widespread presence in packaging, environmental persistence, and the relative maturity of its recovery routes, making it one of the polymers with the highest potential for reincorporation into longer-lifespan technical applications [9]. Experimental studies and reviews on construction materials with recycled PET have documented applications in concretes, mortars, blocks, and panels, showing that performance depends on variables such as substitution percentage, particle size and geometry, matrix type, manufacturing method, and service conditions, and that valorisation is especially promising when waste is integrated into durable products that avoid environmental dispersion and reduce pressure on virgin resources [9–11]. However, most of this evidence has been developed in terrestrial contexts or in applications not subjected to significant coastal loadings; plastic wastes are typically addressed from the logic of recycling, final disposal, or pollution control, while coastal protection and slope stabilisation are habitually treated as hydraulic-structural challenges solved by conventional materials and consolidated typologies [6,10,12,13]. This disciplinary separation restricts the exploration of synergies among waste valorisation, reduced use of virgin materials, and territorial resilience—synergies for which modular systems are particularly relevant, since modularity facilitates localised maintenance, partial replacement, scalability, and progressive adaptation, and the form, interlocking, porosity, and arrangement of modules influence their functional response and material efficiency [14–16]. The use of recycled plastics as slope-stabilisation elements has precedents in geotechnical engineering, where recycled plastic pins have been numerically investigated for highway slopes in expansive Yazoo clay [17]; we extend this line of reasoning to the coastal environment of Chucuito, Callao—the study site and central territorial context of this article—where the slope to be protected sits on the distal deposits of the Rímac–Chillón alluvial fan [18], combines mass-stability demands with wave-induced hydraulic loading, and is exposed to anomalous waves that threaten buildings and infrastructure close to the high-tide line [6,19]. Despite these parallel advances, the literature articulating recycled PET, hollow modular design, coastal stabilisation function, parallel comparative FEA–CFD evaluation, and circularity and embodied-carbon indicators within a single approach remains limited: hydraulic-design frameworks for coastal armour (e.g., van der Meer–Pilarczyk, The Rock Manual, Bruce et al., Burcharth–Hughes) [13–16] do not address recycled-PET incorporation or modular embodied-carbon indicators; studies on PET-incorporated concrete (e.g., Sharma–Bansal, Saikia–de Brito, Akçaözoğlu et al.) [9–11] demonstrate mechanical feasibility in non-coastal applications without coupling hydraulic-attenuation function or cradle-to-gate sustainability accounting; and LCA-oriented works on recycled PET in construction (e.g., Gravina et al. [20]) report embodied-carbon performance for terrestrial applications without articulating the modular-geometry/coastal-stabilisation dimensions.

The research question guiding this work is: to what extent can a hollow modular unit fabricated with a recycled PET–concrete composite, evaluated under a parallel, one-way comparative FEA–CFD scheme, suggest improvements in hydraulic-attenuation performance relative to a conventional rip-rap reference, together with structural-response coherence, material efficiency, plastic-waste valorisation and preliminary embodied-carbon indicators evaluated per modular unit? We hypothesise that the combined hollow geometry and partial recycled-PET substitution reduce the simulated run-up indicators relative to a conventional rip-rap reference, reduce the embodied-CO_2 footprint per functional unit relative to a solid-concrete reference, and increase the volume of post-consumer PET valorised per unit, within the comparative scope of a numerical study. On this basis, the study pursues four specific objectives: (i) to comparatively evaluate the structural response of the proposed unit relative to a control block through FEA, and its hydraulic performance relative to a rip-rap baseline through CFD, at three slope angles; (ii) to quantify circular-economy indicators (material saving and PET-bottle valorisation) per functional unit; (iii) to perform a preliminary cradle-to-gate embodied-CO_2 estimate with sensitivity analysis; and (iv) to define a staged validation roadmap, prioritising the experimental, durability, and economic evaluations required before field deployment.

We address this gap by combining recycled-PET valorisation and hollow modular geometry for coastal protection with a comparative, parallel one-way FEA–CFD assessment, benchmarked through an explicit EurOtop-based run-up analysis and a contextual order-of-magnitude comparison with van der Meer-related armour-stability literature, and by connecting the simulation outputs with unit-level circularity indicators and a preliminary cradle-to-gate embodied-carbon assessment for a vulnerable Latin-American coastal setting, in dialogue with SDG 11, SDG 12, and SDG 13. To our knowledge, few studies have examined this combination of recycled-PET valorisation, hollow modular coastal-protection geometry, comparative numerical hydraulic assessment, and sustainability indicators within the same study. We present the results as a screening-level numerical evidence base intended to motivate, not to replace, the experimental and field validation required before any deployment.

2. Materials and Methods

The methodology was structured to relate the territorial diagnosis of the site, the geometric definition of the module, the parametrisation of the PET–concrete composite, and the comparative numerical evaluation under equivalent loading conditions. The following subsections describe the procedure followed and the assumptions adopted to ensure trace-

https://doi.org/10.3390/su18168201

ability and comparability among configurations. The study is presented as an exploratory numerical evaluation based on a structural model with an equivalent hydrodynamic load; consequently, the results must be interpreted within the model assumptions and not as a definitive validation of hydraulic design.

2.1. Site Selection

The site selection for the unit's implementation was carried out within the coastal edge of Chucuito, based on criteria of marine exposure, evidence of local erosion, proximity to the coastline, and relevance of the location for evaluating the modular system's performance under real conditions. The geographical location of the study area is shown in Figure 1, which contextualises the site within South America, Peru, the province of Callao, and the Chucuito coastal edge in the district of Callao. Rather than considering the study area as a homogeneous front, a qualitative zoning of the littoral was established according to its relative level of exposure to incident waves and its relationship with visible processes of erosion and undermining.

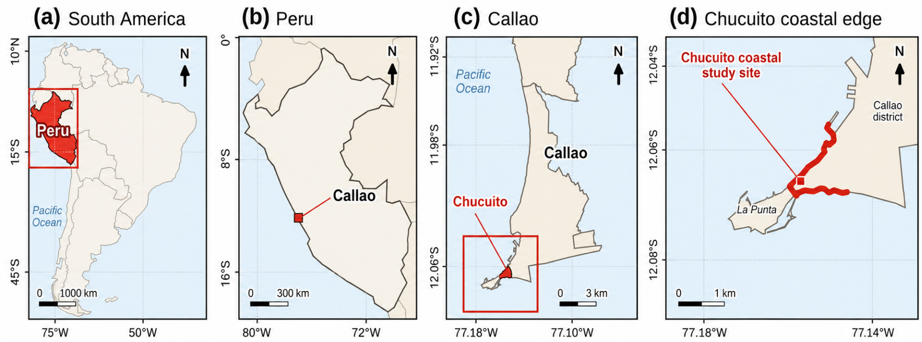

Figure 1. Geographical location of the study area at four nested scales: (**a**) South America; (**b**) Peru; (**c**) Callao province; (**d**) the Chucuito coastal edge, located in Callao district, adjacent to La Punta.

Based on this territorial reading, the Chucuito coastal front was adopted as the study area, based on its direct exposure to incident waves and on visible evidence of shoreline erosion and undermining along the foreshore. The Urb. Chucuito has been formally identified as a high-risk sector for anomalous wave events in the official risk assessment prepared by the Regional Government of Callao [21], which provides the institutional and territorial reference for the area selected here. For the screening-level evaluation, the most exposed segment of this front was adopted as the representative siting condition for the modular unit; site-specific quantitative characterisation of wave-energy distribution along the broader Chucuito front is identified as future work.

2.2. Study Design and Methodological Scope

This study was designed as a comparative engineering evaluation aimed at analysing, under equivalent conditions, the technical performance and circularity potential of a modular system fabricated with a PET–concrete composite proposed for coastal slope protection and stabilisation in Chucuito–Callao. We designed the methodology to compare different geometric configurations without altering the unit's external volume or the reference loading condition so that the observed effect could be attributed mainly to the unit's form and material efficiency.

The comparative configurations were defined by three slope-base angles (60°, 53°, and 45°), in addition to a conventional control configuration; the modular-unit geometry was treated separately from the tested slope configuration. The response variables were the maximum displacement, the residual rigid-body kinetic energy after impact (Section 2.11), a qualitative structural-response screening, and a set of circular-economy indicators per functional unit. The evaluation was implemented through finite-element numerical modelling in SolidWorks Simulation Premium 2018 in combination with a companion CFD analysis (Section 2.9) under an equivalent hydrodynamic load. The structural-response screening is qualitative in the sense that it tracks order-of-magnitude bounds on displacement, residual kinetic energy, and structural-response coherence among configurations under the adopted basal restraint, rather than reporting site-specific stress, crack-pattern, or factor-of-safety values; the latter would require site-specific loading and is identified as future work. This section is limited to describing materials, parametrisation, boundary conditions, numerical protocol, and evaluation metrics, without anticipating the interpretation of results.

2.3. Materials and Characterisation of the PET–Concrete Composite

Post-consumer polyethylene terephthalate (PET) sourced primarily from 3 L recycled bottles was used, selected for its low water absorption, local availability, and reported mechanical behaviour for applications requiring durability. The PET was processed as mechanically shredded post-consumer flakes with a nominal particle size in the range 4–10 mm, a design choice of this study; reported PET-aggregate granulometries in the reference literature are generally finer (e.g., 0–4 mm granules in [11]; see also the review in [9]). The reference cementitious material was defined as a conventional mortar-grade matrix of sand, cement, and water with a target compressive strength of approximately 21–28 MPa (equivalent to a low-strength structural concrete class), with fine granulometry aligned with NTP 400.012 [22]. A target mix of 10% PET and 90% cementitious matrix by volume was adopted, with an acceptable operating range of 8–10% (volume-based), informed by previous tests on PET-incorporated cementitious mixes [9,11]. In this configuration, PET in the form of shredded post-consumer flakes partially replaces the volume of the cementitious matrix; it is not introduced as a substitute for cement clinker nor as a fine-aggregate replacement in a strict mix-design sense, but as a volumetric fraction of the consolidated matrix. The optimal dosage for marine exposure has not been established and is identified as a research priority (Section 4.9). The PET mechanical properties listed in Table 1 are reported for completeness and refer to the PET phase as a continuous polymer (e.g., compressive strength of moulded post-consumer PET specimens) rather than to the shredded-flake form actually used in the composite; in the consolidated composite, the load-bearing role of the PET fraction is constrained by the cementitious matrix, by polymer creep, and by the relatively low glass-transition temperature of PET ($T_g \approx 75$ °C), and consolidated composite properties are reported in the last column of Table 1.

Table 1. Consolidated physical–mechanical properties used as input for the study.

Property	Post-Consumer PET	Cementitious Control	PET–Concrete Mix (10/90)
Density (kg/m^3)	1335	2400	≈2250
Compressive strength (MPa)	76–128	21–28	21.5
Flexural strength (MPa)	15.55	3.5–4.5	5.2
Modulus of elasticity (GPa)	2.0–3.0	25–30	≈22
Water absorption (%)	Negligible	—	≤6

For numerical-modelling purposes, the PET–concrete composite was represented as an equivalent isotropic solid. This decision avoids introducing unverifiable assumptions about local detachments or heterogeneities at the PET–matrix interface and maintains comparability among geometric configurations. Consequently, the model does not consider an internal bonded contact between PET and concrete; instead, consolidated equivalent properties are used for the entire mixture (Table 1).

This idealisation does not represent PET–matrix bonding and debonding, interfacial transition-zone behaviour, or the local stress concentrations that arise around PET flakes and may therefore underestimate the risk of local failure initiation at the interface, even where global demands remain low. Published micromechanical and pull-out evidence for PET-modified cementitious composites indicates that the PET–matrix interface is typically the weakest link of the composite, with single-fibre pull-out tests showing that bond behaviour is governed by fibre shape and surface characteristics [23,24]. Consequently, the FEA results reported in this study should be read as global indicators (peak displacement, residual kinetic energy) of the unit's transient response, not as local-failure predictions; interface-level assessment requires the mix-specific bond–shear characterisation identified in the validation roadmap (Section 4.9). The required mix-specific bond–shear characterisation was not available for the present study; this gap is stated explicitly here and in Section 4.8, and the published values above are used to bound the expected effect.

The justification of the input values in Table 1 is as follows: the 10% volumetric PET dosage was informed by experimental characterisations of PET-incorporated cementitious mixes reporting acceptable strength and water-absorption performance [9,11], and the mechanical properties in Table 1 are adopted screening values informed by the ranges reported in that literature, pending the experimental characterisation identified in Section 4.9.

2.4. Modular Unit, Geometry and Compared Configurations

The functional unit adopted was one hollow modular unit of 1 m^3 external volume. The unit was modelled as a 1 m-edge cube incorporating a hollow multi-opening geometry with nominal 0.60 m circular openings connected through an internal void; the hollow geometry was designed to reduce material volume and is hypothesised to influence energy redistribution during wave impact, although this redistribution effect was not directly measured in the present screening-level analysis and remains to be characterised experimentally. To isolate the geometric effect, all cases preserved the same external volume and the same general loading scheme. The 7 m and 6 m inclined reference dimensions shown in Figure 2 correspond specifically to the 53° configuration. Their vertical projections are approximately 5.6 m and 4.8 m, respectively, defining the reference defence height H = 10.4 m used in the numerical domain. Across the 60°, 53°, and 45° slope configurations, H = 10.4 m was retained, while the corresponding inclined lengths vary with slope angle. The A = 6 m^2 area used in Equation (1) was retained as a fixed reference load-definition area based on the 6 m × 1 m upper armoured-face reference of the 53° configuration, rather than as an angle-dependent projected area. Figure 2 illustrates the cross-section configuration of the modular system arranged along a 53° slope, with geometric references. It is acknowledged that, for any direct comparison with rip-rap as a complete coastal-defence solution, a more appropriate functional unit would be defined per linear metre of protected coastline at an equivalent protection level; this is identified as a limitation of the LCA and economic analysis (Sections 3.7, 4.6 and 4.8).

Three slope configurations associated with base angles of 60°, 53°, and 45° were evaluated, in addition to a control block of conventional geometry. The control was used as a baseline for the comparative assessment of the mechanical response to impact and the system's material efficiency.

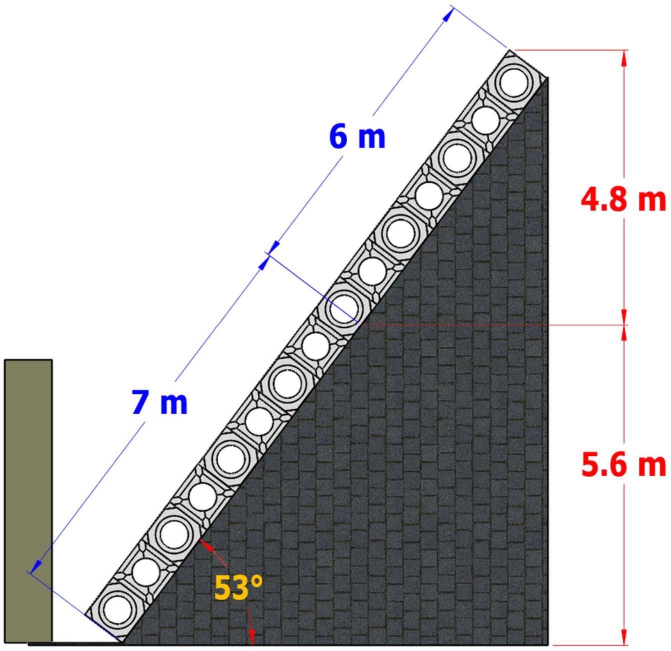

Figure 2. Cross-section schematic of the proposed modular coastal defence: hollow PET–concrete units arranged along the 53° reference slope configuration. The 7 m lower and 6 m upper dimensions are inclined reference lengths measured along the 53° slope; their vertical projections are approximately 5.6 m and 4.8 m, respectively, defining the total reference defence height H = 10.4 m.

2.5. Geotechnical Setting and Baseline Stability of the Unprotected Slope

The Chucuito foreshore lies on the distal, coastal edge of the Quaternary Rímac–Chillón alluvial fan, the fan-delta system on which metropolitan Lima and Callao are built [18,25]. Whereas central Lima is founded on the thick, dense gravel of the fan (the "Lima Conglomerate"), towards the Callao–La Punta sector, these gravels lose thickness and are overlain by superficial fine-grained deposits, loose to medium silty sands and fines of alluvial and marine origin, a contrast documented since the first seismic-microzonation studies of the area [26–28]. The official risk-assessment report for Chucuito likewise maps the site on low-lying marine-terrace and alluvial-fan deposits [21]. These conditions, non-cohesive or weakly cohesive granular soils on a highly seismic coast, define the geotechnical relevance of surface protection for the studied slope.

To establish a baseline for the protected configurations, following the approach of reference stability studies with recycled-plastic elements [17], a screening-level limit-equilibrium stability analysis of the unprotected slope was performed using the simplified Bishop method [29] with circular slip surfaces, for the same slope height adopted in the numerical domain (H = 10.4 m, consistent with the reference dimensions of Figure 2) and the three inclinations studied (θ = 45°, 53° and 60°). Two representative material sets were considered, bounding the local stratigraphy (Table 2): Soil A, a surficial silty sand representative of the distal-fan/marine-terrace cover (γ = 18 kN/m^3, c' = 5 kPa, φ' = 31°), and Soil B, the dense gravelly fan deposit (γ = 20.5 kN/m^3, c' = 15 kPa, φ' = 39°). These parameters are adopted as screening values consistent with the ranges reported for the local units in the cited studies; as the site risk assessment [21] does not report laboratory geotechnical parameters, the values adopted here are screening estimates based on the regional literature [26–28] and should be refined with site-specific laboratory or in situ testing; the analysis assumes dry, homogeneous conditions. Static and pseudo-static cases were analysed, the latter with a horizontal seismic coefficient kh = 0.5·Z = 0.225, adopted following common Peruvian geotechnical practice, with Z = 0.45 for seismic zone 4 per E.030 [30], and results were compared against the minimum factors of safety (FS) required by the Peruvian slope-stabilisation standard (FS $\geq$ 1.5 static; FS $\geq$ 1.25 pseudo-static) [31]. The slice discretisation and critical-surface search settings of the limit-equilibrium analysis are not individually reported; the FS values in Table 3 are therefore screening-level results whose qualitative pattern, rather than their exact decimal values, supports the conclusions drawn here. The scripts implementing this limit-equilibrium calculation were developed with the support of a generative AI assistant (Claude Sonnet 4.5, Anthropic). The underlying equations, input parameters and outputs were reviewed and verified by the authors before use (see also the Acknowledgments Section).

Table 2. Adopted screening-level geotechnical parameters for the baseline stability analysis of the unprotected slope.

Parameter	Soil A—Surficial Silty Sand	Soil B—Dense Gravelly Fan Deposit	Basis
Unit weight γ (kN/m^3)	18.0	20.5	Adopted screening value
Effective cohesion c' (kPa)	5	15 (apparent)	Adopted screening value
Friction angle φ' (°)	31	39	Range for local units [26–28]
Groundwater	Dry	Dry	Screening assumption
Seismic coefficient kh	0.225	0.225	0.5·Z, Z = 0.45 [30]

The computed factors of safety for the three inclinations and the two bounding material sets are summarised in Table 3.

Table 3. Factors of safety of the unprotected slope (simplified Bishop method, dry homogeneous conditions).

θ (°)	Soil A—Static	Soil A—Pseudo-Static	Soil B—Static	Soil B—Pseudo-Static
45	1.11	0.81	1.77	1.30
53	1.01	0.77	1.62	1.25
60	0.98	0.77	1.57	1.24

The unprotected slope is marginal to unstable across the studied range. For Soil A, the static factor of safety is marginal, approaching or falling below unity at the steeper angles (FS $\approx$ 1.11, 1.01 and 0.98 at 45°, 53° and 60°), and drops to 0.77–0.81 under pseudo-static loading, i.e., failure is predicted under the design earthquake. For the favourable Soil B, the static factors (1.57–1.77) satisfy the normative requirement, but the pseudo-static factors (1.24–1.30) are at or marginally below the required 1.25, with FS = 1.24 at θ = 60° falling slightly below the requirement [31]. The unprotected slope therefore does not provide normative stability margins under the site's seismic demand, which motivates the evaluation of surface-protection concepts potentially relevant to subsequent slope-stabilisation strategies, such as the proposed modular unit.

Figure 3 presents the critical slip surfaces at the design inclination θ = 53°, following the presentation format of reference numerical slope-stabilisation studies [17].

The critical surfaces are toe circles that daylight on the upper ground surface just behind the crest, i.e., potential failures involve the full slope face rather than shallow skin instabilities; under pseudo-static loading, the critical circle for Soil A becomes marginally deeper while its factor of safety drops well below unity (0.77), indicating that seismic action, rather than gravity alone, governs the stability of the unprotected slope. It should be noted that this limit-equilibrium analysis addresses mass slope stability under gravity and seismic loading, which is complementary to, and independent of, the structural and hydraulic performance of the proposed surface-protection concept evaluated with the FEA–CFD framework; direct quantification of the change in global slope factor of safety after installation would require a coupled geotechnical assessment of the protected slope and remains part of the validation roadmap (Section 4.9).

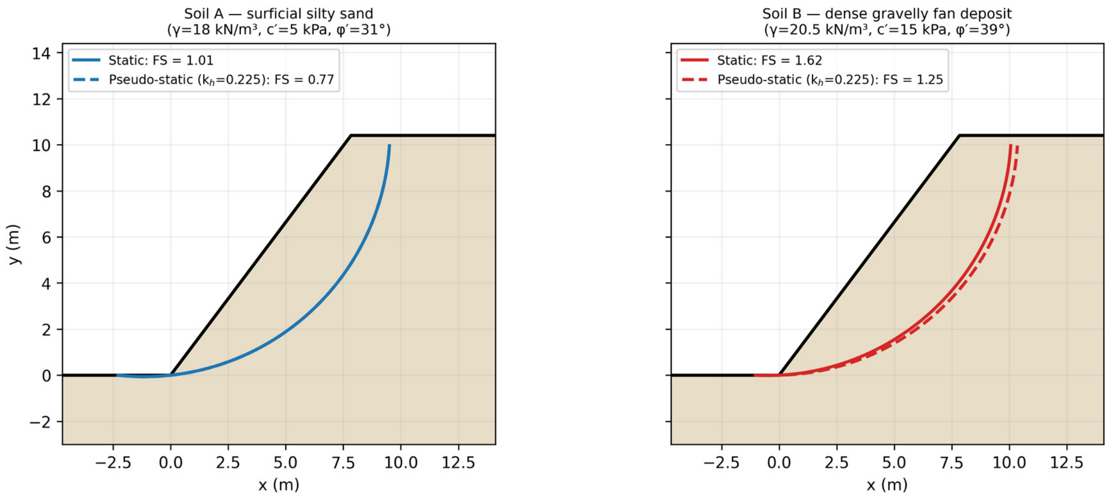

Figure 3. Critical slip surfaces and factors of safety of the unprotected slope at θ = 53° (simplified Bishop method [29], circular slip surfaces, H = 10.4 m, dry homogeneous conditions) for the two bounding material sets under static and pseudo-static (kh = 0.225 [30]) loading. For Soil A, the static and pseudo-static critical surfaces nearly coincide, so the dashed pseudo-static curve overlaps the continuous static one.

2.6. Hydrodynamic Context and Reference-Load Definition

The hydrodynamic context was characterised from two open official sources. First, reports of the Peruvian Directorate of Hydrography and Navigation (HIDRONAV) for the Peruvian Pacific coast describe the anomalous-swell regime affecting the study area [19]; in those reports, sustained wind speeds of the order of 36 knots (≈18.5 m/s), adopted here as a screening value informed by HIDRONAV bulletin practice, are associated with the most energetic swell-generating conditions. This value is a meteorological triggering indicator of swell-generating conditions and should not be interpreted as a water-flow velocity. Second, and as the primary site-specific hydrodynamic reference, the Delft3D inundation modelling commissioned by the Regional Government of Callao for the Chucuito foreshore [21] reports, for input wave heights of Hs = 2.0 m and Hmax = 3.5 m derived from the Directorate's hydrographic wave reanalysis (HIDRONAV), maximum inundation flow velocities of 5 m/s at the Cantolao and Arrieta beaches, velocities of the order of 3–4 m/s at the José Gálvez and Santa Rosa squares, and maximum inundation depths of 4 m.

On this basis, the comparative evaluation adopts equivalent inlet peak velocities of 3, 5 and 7 m/s as realistic loading scenarios: the 5 m/s case reproduces the maximum flow velocity of the site-specific model, while 3 and 7 m/s bracket it to capture moderate and above-maximum conditions. A 10 m/s case is retained as a conservative upper-bound scenario, approximately twice the site-modelled maximum. Within the 3–7 m/s velocity-sensitivity series, the slope geometry, mesh family and boundary-condition types were retained; only the inlet velocity was varied. The separate 10 m/s conservative angle-comparison run set is distinguished in Sections 2.9 and 3.5. These values should be understood as equivalent CFD inlet velocities and FEA impact-velocity references adopted for controlled comparison, not as probabilistic representations of the local wave climate; future work should evaluate the unit under irregular wave trains, multiple periods and incidence directions consistent with the local climate. The conversion from wave parameters to an equivalent peak inlet velocity is an idealisation adopted to enable cross-configuration comparisons rather than a formal hydraulic-design calculation.

Accordingly, wave action was represented by an equivalent time-dependent lateral force applied to the exposed face of the unit. The adopted formulation is the standard quadratic drag form for blunt bodies subjected to flow [13,32]:

$$F(t) = 0.5\,\rho\,C_d\,A\,v(t)^2 \quad (1)$$

where F(t) is the equivalent hydrodynamic impact force applied to the exposed face of the unit, ρ = 1025 kg/m^3 corresponds to the standard seawater density [13], C_d = 1.5 is the drag coefficient adopted for cube-like blunt bodies under transient impact conditions, with 1.05–2.0 taken as sensitivity bounds spanning values commonly reported for cube-like bluff bodies in the hydraulic-structures literature (Table 4), A = 6 m^2 is the fixed reference load-definition area adopted from the 6 m × 1 m upper armoured-face reference of the 53° configuration (Figure 2) and retained across slope configurations for controlled comparative FEA loading, and $v(t)$ is the equivalent impact velocity history, defined as the triangular pulse of the following equation:

$$v(t) = v_{peak}\cdot(t/t_{rise})\ for\ 0 \le t \le t_{rise};\ \ v(t) = v_{peak}\cdot(t_{total} - t)/(t_{total} - t_{rise})\ for\ t_{rise} < t \le t_{total};\ \ v(t) = 0\ otherwise$$

where v_{peak} is the scenario peak velocity (3, 5, 7 and 10 m/s), t_{rise} = 0.25 s is the time to peak, and t_{total} = 0.5 s is the total pulse duration; this idealisation condenses the rise–peak–decay pattern of an impacting wave front into a tractable transient pulse. Because F ∝ v^2, the corresponding peak loads $F_p = 0.5\cdot\rho\cdot C_d\cdot A\cdot v_{peak}^2$ are 41.5, 115.3, 226.0 and 461.3 kN for 3, 5, 7 and 10 m/s, respectively; within each scenario, the same load function was applied to all configurations to preserve comparability among geometries. This design impact load, the local structural demand acting on the armoured face and used as input to the FEA, is conceptually distinct from the total hydrodynamic force integrated by the CFD solver over the entire submerged boundary of the domain, which is dominated by the hydrostatic component and is one to two orders of magnitude larger; the two quantities describe different actions (a local impact demand versus a global boundary force) and are therefore not interchangeable. Applying the load associated with the full armoured face (A = 6 m^2) to an individual 1 m^3 unit constitutes a deliberately conservative per-unit structural demand for screening purposes, since in the assembled system, this load would be shared among the units of the face. Under linear shallow-water theory, the celerity at the breaking depth h ≈ 1.3 m adopted for the study area is c = (g·h)^0.5 ≈ 3.6 m/s; the site-referenced scenarios therefore correspond to Froude numbers of approximately 0.8–2.0 with respect to c, while the conservative 10 m/s scenario corresponds to a high-Froude transient impact event (Fr ≈ 2.8) representative of breaking-induced impulsive loading rather than a steady ambient condition.

Table 4. Parametric sensitivity of the peak impact load F (Equation (1)) to the drag coefficient C_d across the four velocity scenarios. C_d = 1.05 and C_d = 2.00 represent the lower and upper bounds, respectively, of the range adopted for sensitivity screening (Section 2.6), while C_d = 1.50 is the central value used in this study.

V (m/s)	F, Cd = 1.05 (kN)	F, Cd = 1.50, Adopted (kN)	F, Cd = 2.00 (kN)	Variation vs. Central
3	29.1	41.5	55.4	−30%/+33%
5	80.7	115.3	153.8	−30%/+33%
7	158.2	226.0	301.3	−30%/+33%
10 (cons.)	322.9	461.3	615.0	−30%/+33%

This representation is an equivalent loading scheme rather than a definitive hydraulic design input. It does not capture irregular wave trains, oblique incidence, infragravity waves, breaking-induced impulsive pressures, or sediment transport, all of which would require dedicated hydraulic-design analysis and physical-model testing. Within the comparative scope of this study, the formulation is appropriate for ranking configurations under identical assumptions; it should not be used to prescribe armour weights, freeboard, or structural sizing for site implementation, which would require van der Meer–type stability analysis [14,33] and EurOtop overtopping criteria [34], complemented by physical-model tests.

All configurations evaluated in this work share the same external footprint (1 m × 1 m × 1 m unit on a slope of identical defence height H = 10.4 m), the same equivalent loading function, and the same fluid properties. As a consequence, the relevant non-dimensional groups governing the comparison (Froude number based on the inlet velocity and the unit edge length, Reynolds number based on the same length and the kinematic viscosity of seawater, and the geometric ratio between the cavity diameter and the unit edge) remain identical across configurations. The comparative reading of the results is therefore preserved at the prototype scale used in the simulation; transfer to a small-scale physical model would require explicit Froude-similarity scaling and is identified as a follow-up step in Section 4.9.

The sensitivity of the peak impact load to the adopted drag coefficient was assessed parametrically across the reported range for cube-like blunt bodies (C_d = 1.05–2.0; Table 4). Because $F \propto C_d$ in Equation (1), the variation in peak load is proportional and uniform across the four velocity scenarios: adopting C_d = 1.05 reduces the peak load by approximately 30% relative to the central case, while C_d = 2.00 increases it by approximately 33% (Table 4). The CFD run-up indicators are independent of C_d, as the inlet velocity is prescribed directly as a boundary condition in the CFD solver and is not derived from Equation (1). Within the FEA component, variation of C_d changes the magnitude of the equivalent load defined by Equation (1). The parametric assessment reported here therefore quantifies load-input sensitivity to C_d; it does not independently quantify changes in the structural-response indicators across C_d values.

2.7. Numerical Finite-Element Model Configuration

The FEA component is used in this study as a structural-response screening tool rather than as a full structural-design verification. Simulations were performed with SolidWorks Simulation Premium 2018 by means of a transient nonlinear dynamic analysis. This type of analysis allows for representing large displacements, frictional contact, and time evolution of the system response after impact. The governing equation solved by the software corresponds to the classical matrix form of dynamic equilibrium (Equation (2)):

$$M\ddot{u} + C\dot{u} + Ku = F(t) \tag{2}$$

where M, C and K are the mass, damping, and stiffness matrices, respectively; u, $\dot{u}$ and $\ddot{u}$ are the nodal displacement, velocity and acceleration vectors, respectively; and $F(t)$ is the external-load vector [35], written here in the bracket-free matrix notation of [35], with the load vector denoted F(t) for consistency with Equation (1). Time integration was carried out using the implicit Newmark method with β = 0.25 and γ = 0.5, a time step of 0.001 s, and a total duration of 2.0 s. The 2.0 s window covers the 0.5 s impact pulse plus a 1.5 s post-impact response interval, which is sufficient to capture the peak structural response and the subsequent decay of residual kinetic energy for an individual unit subjected to a single transient pulse. This window is not intended to represent the full transient evolution of the free-surface flow in the CFD analysis, where run-up indicators were read from converged velocity-field cut-plots (Section 2.9).

2.8. Damping, Contact, Boundary Conditions and Mesh

Energy dissipation was modelled through Rayleigh damping ($C = \alpha M + \beta K$, with coefficients $\alpha = 0.15$ and $\beta = 2 \times 10^{-5}$ adopted for a target modal damping ratio of 3%). A frictional unit–substrate contact definition ($\mu = 0.45$, representative of a concrete-on-densely-packed-granular-substrate interface) was also included in the model. The bottom face of the unit was modelled with basal restraint, consistent with the screening-level scope of the analysis; under this restraint, interface sliding does not develop, so frictional contact is not counted among the active dissipation mechanisms of the reported analyses. Because the base is restrained, the resulting structural-response indicators (Sections 2.11 and 3.4) provide relative comparisons among configurations under this common boundary condition, rather than an independent test of resistance to overturning or basal separation, which would require a boundary condition that leaves these degrees of freedom free to develop (Section 4.9). Site-specific values of μ for saturated or rocky substrates require geotechnical characterisation and are identified as future work. The mesh was generated with parabolic 10-node tetrahedral elements with a global maximum size of 10 mm and local refinement to 0.5 mm at edges and the internal cavity; mesh independence was verified by a four-level refinement study (20–15–10–8 mm) yielding strain-energy variations below the adopted 2% convergence threshold between the 10 mm and 8 mm levels.

2.9. Companion Computational Fluid Dynamics Analysis

Complementary to the structural analysis, a companion computational fluid dynamics (CFD) analysis was carried out using SolidWorks Flow Simulation to estimate the run-up flow velocity and the maximum free-surface elevation along the slope-defence profile. This step was required because the equivalent-load formulation in Equation (1) yields the impact force on a single unit but does not, by itself, provide the run-up height or the velocity field along the slope. The two analyses were therefore organised as a parallel, one-way comparative FEA–CFD framework rather than as a coupled fluid–structure interaction (FSI): the FEA (Sections 2.7 and 2.8) provides the structural-response screening of an individual hollow unit under the equivalent impact load, while the CFD analysis described here provides the macroscopic flow indicators reported as run-up velocity and water-surface elevation in Section 3. No bidirectional FSI is performed, and no iterative passing of pressures between solver and structure is implemented; both analyses use consistent geometric configurations and reference peak velocities but are otherwise independent.

SolidWorks Flow Simulation 2018 was selected for this companion analysis on the basis of three considerations: (i) compatibility with the same geometric models used in the FEA, which simplifies the workflow and ensures geometric consistency between both analyses; (ii) availability and accessibility within the design environment used for the modular unit; and (iii) the comparative, rather than predictive, scope of the present study, in which, within each run set, all configurations are evaluated under identical solver assumptions, so that any solver-induced bias is expected to affect the compared cases similarly. The solver choice is therefore justified for comparative consistency across configurations rather than for high-fidelity coastal prediction. Previous peer-reviewed studies have employed SolidWorks Flow Simulation for external-flow and hydraulic problems [36,37], which supports its use within the comparative scope declared here. More specialized hydraulic-engineering codes (e.g., OpenFOAM with interFoam, ANSYS Fluent, FLOW-3D, or Delft3D-FLOW) offer more advanced free-surface treatments and turbulence models and would be appropriate for a definitive hydraulic-design step or for high-fidelity coastal modelling; their use is identified as a follow-up task in Section 4.9.

The CFD model solves the Reynolds-Averaged Navier–Stokes (RANS) equations with the k–ε turbulence closure as implemented in SolidWorks Flow Simulation and tracks the air–water interface through the free-surface (Volume-of-Fluid-type, VOF) formulation as implemented in the solver. The computational domain (Figure 4e) reproduces the slope cross-section shown in Figure 2, with a defence height H = 10.4 m and a water depth representative of the Chucuito–Callao foreshore (≈1.3 m at the breaking line; see Figure 5). A uniform inflow velocity is prescribed normal to the offshore boundary, in line with the loading scenarios of Section 2.6 (3, 5 and 7 m/s at θ = 53° and 10 m/s as the conservative scenario at the three slope angles); the outflow is set as static pressure. A no-slip condition is applied to the slope surface. The solver domain is three-dimensional, as documented in the solver project reports and rendered isometrically in Figure 4e; the flow configuration is nevertheless cross-sectional in character, with no lateral variation imposed on the incident flow. Both armour conditions are represented with hydraulically smooth surfaces in the CFD model: the rip-rap baseline is idealised as a plane smooth slope, whereas the hollow-unit configuration explicitly resolves the module geometry on the slope face. Surface roughness is therefore not imposed as a boundary-condition parameter in any of the runs (original or velocity-sensitivity); because the CFD deliberately omits wall roughness, its influence is complemented analytically through the EurOtop-based assessment of Section 2.10 (roughness influence factors, Table 5, and the run-up benchmark and roughness-sensitivity analysis, Tables 6 and 7), and the differences observed between the two CFD configurations arise from the resolved geometry of the unit rather than from a prescribed roughness coefficient. The cross-sectional flow configuration, the RANS k–ε closure, and the smooth-surface idealisation are simplifications appropriate for a comparative screening, but they do not capture wave obliquity or alongshore variability, anisotropic turbulence near the breaking zone, or pore-scale flow within and between individual units.

The equivalent roughness/influence factors used in the analytical assessment are the tabulated values of EurOtop [34]: γf = 0.40–0.55 for two-layer rock armour (permeable and impermeable core, respectively), γf = 1.0 for smooth slopes, and an adopted range of γf = 0.70–0.90 for the hollow PET–concrete unit, bounded between smooth block revetments and textured armour layers; the latter is a declared screening assumption pending experimental calibration, since no tabulated value exists for the proposed geometry (Table 5). EurOtop additionally prescribes that the influence of roughness decreases for large breaker parameters, with γf increasing linearly towards 1.0 between $\xi m - 1{,}0 = 1.8$ and 10 (where $\xi m - 1{,}0 = \tan\alpha/\sqrt{(Hm0/Lm - 1{,}0)}$ is the breaker parameter, formally presented in Section 2.10) and roughness having no residual influence for $\xi m - 1{,}0 \geq 10$ [34].

Table 5. Roughness influence factors adopted for the analytical assessment. The rock-armour values originate from EurOtop's rubble-mound chapter (Table 6.2) and the basalt/block-revetment value from the dike chapter (Table 5.2); the two sets address different structure types and are combined here for indicative screening only.

Surface/Armour Type	γf (EurOtop 2018, Tables 6.2 and 5.2) [34]	Role in This Study
Smooth concrete/smooth slope	1.00	CFD idealisation of both configurations
Rock, two layers, permeable core	0.40	Lower bound, rip-rap reference
Rock, two layers, impermeable core	0.55	Upper bound, rip-rap reference
Basalt/block revetments (reference)	0.90	Upper bound of the adopted unit range
Hollow PET–concrete unit (this study)	0.70–0.90 (adopted assumption)	Declared screening assumption, pending experimental calibration

https://doi.org/10.3390/su18168201

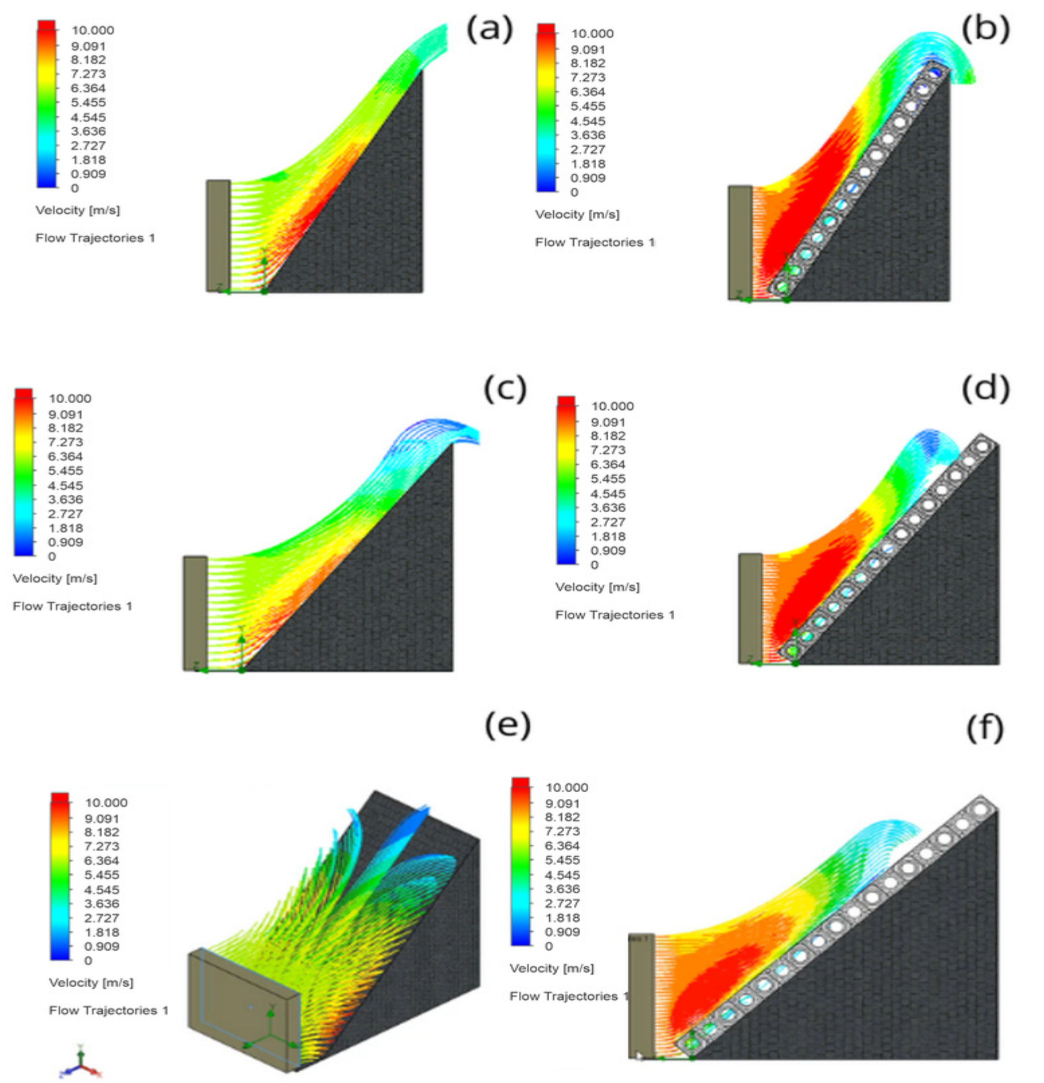

Figure 4. Comparative CFD simulation results (SolidWorks Flow Simulation 2018) for three slope-base angles, showing the run-up flow field along the protected slope. (**a**) Rip-rap defence at θ = 60°; (**b**) hollow PET–concrete units at θ = 60°; (**c**) rip-rap defence at θ = 53°; (**d**) hollow PET–concrete units at θ = 53°; (**e**) rip-rap defence at θ = 45°; (**f**) hollow PET–concrete units at θ = 45°. The colour scale on each panel represents the flow-velocity magnitude (m/s); all panels share a common, manually fixed colour scale (0–10 m/s) so that a given colour corresponds to the same velocity in every panel and colours are directly comparable across configurations. Model defence height H = 10.4 m. Numerical run-up velocity ranges and maximum free-surface elevations corresponding to each panel are reported quantitatively in Table 8. Panels are SolidWorks flow-trajectory visualisations (solver label "Flow Trajectories 1"); panel (**e**) is rendered as an isometric view of the solver domain, whereas the remaining panels are lateral views. The numerical indicators in Table 8 were extracted from velocity-field cut-plots (Section 2.11), not from these trajectory renderings.

The domain was discretised with an adaptive Cartesian mesh refined near the slope and the free surface. The mesh density was set through the solver's adaptive refinement control rather than by a fixed cell count, so that the resolution adapts to the flow gradients of each configuration; in the velocity-sensitivity runs, the mesh comprised 290,450 cells for the hollow-unit configuration and 571,740 cells for the rip-rap baseline, the finer rip-rap mesh reflecting the solver's adaptive refinement response in that configuration; the initial angle-comparison runs used comparable resolutions (of the order of 1.8–2.4 $\times$ 10^5 cells). All cases used a common computational-domain framework—the same boundary-condition types and the same refinement strategy; cell counts varied according to the tested configuration and the solver's adaptive refinement response. The finer meshes used in the velocity-sensitivity runs (executed with SolidWorks Flow Simulation 2025, as documented in the corresponding project reports) reduce discretisation error relative to the angle-comparison meshes; a dedicated CFD mesh-convergence dataset is not reported in the main text, and quantitative comparison across the two run sets is therefore not intended (Section 3.5). Run-up velocities were read from the converged velocity-field cut-plots along the slope profile, and the corresponding maximum free-surface elevations were obtained trigonometrically from the run-up length measured along the slope hypotenuse. These post-processing readings provide profile-scale indicators for comparison between configurations rather than probe-point solver outputs; their consistency with the independent EurOtop-based estimates (Section 2.10) supports their use at this screening level. The model evaluates a single unit type along an idealised slope profile and does not represent inter-unit interaction, interlocking effects, progressive displacement or dislodgement of individual units, armour-layer failure, toe stability, or scour at the base of the structure; these phenomena require dedicated coupled hydraulic–geotechnical modelling (e.g., coupled CFD–discrete element method (DEM) simulation of an armour panel) and physical-model testing, and are not addressed in the present study. The unit is conceived for row-wise pattern placement on the slope with face-to-face contact between adjacent cubes, following the logic of pattern-placed single-layer cube armour and modern regular-placed interlocking armour systems [38,39], in which armour-layer stability derives from unit weight, inter-unit friction and geometric interlocking and is strongly dependent on placement pattern and packing density [38]. In the current concept, no additional shear keys, interlocking recesses or inter-row overlaps are introduced; stability therefore relies on unit self-weight and face-to-face friction between adjacent units, while quantitative assessment of multi-unit interaction and connection mechanisms constitutes the next stage of the validation roadmap (Section 4.9).

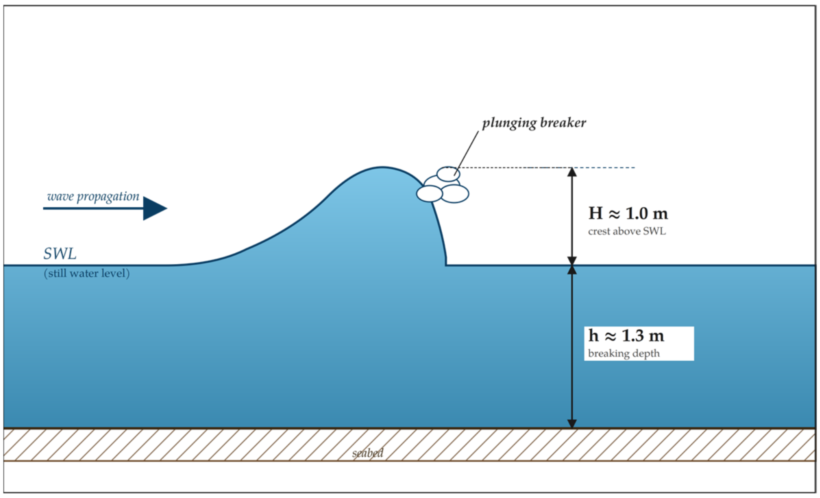

Figure 5. Schematic representation of the wave-breaking condition at the adopted screening depth of approximately 1.3 m for the Chucuito–Callao foreshore. The screening context is informed by open coastal-environment information published by the Directorate of Hydrography and Navigation (HIDRONAV) of the Peruvian Navy [19]; the depth and schematic breaking-zone configuration are modelling assumptions adopted for the present comparison. The figure is a conceptual sketch produced by the authors and is not a verbatim reproduction of any HIDRONAV figure; the indicative wave height annotated in the sketch (H $\approx$ 1.0 m) is likewise an adopted screening value rather than a specific published measurement.

2.10. Internal Verification, Comparative Consistency Check and Analytical Benchmark

Because no full-scale or laboratory data of the proposed unit are yet available, we assessed the model through five complementary checks: (i) energy balance of the FEA; (ii) analytical contrast for the structural response; (iii) mesh independence; (iv) a qualitative comparison of the rip-rap CFD output against indicative ranges from established coastal-engineering frameworks; and (v) an analytical benchmark of the CFD free-surface elevations against the EurOtop run-up formulations. These checks are intended for internal verification and comparative consistency only; they do not constitute hydraulic validation, which would require physical-model testing under regular and irregular wave conditions.

First, the FEA energy histories, including kinetic energy, strain energy, and damping-dissipated work, were inspected as an internal numerical-consistency check during the simulation. Second, the control-block response was compared qualitatively with a simplified rigid-body analytical estimate as an order-of-magnitude consistency check. These checks were used to screen numerical behaviour rather than as formal quantitative verification. Third, mesh independence was confirmed by the convergence test described in Section 2.8, with strain-energy variation below 2% between 10 and 8 mm element sizes.

Fourth, the CFD-predicted run-up velocities for the conventional rip-rap configuration were subjected to an order-of-magnitude consistency check against flow regimes associated with van der Meer armour-stability and run-up-related conditions [14,33,40]. In this fourth check, van der Meer [14,33,40] is used as a contextual reference for the rip-rap run-up velocities rather than as a formulation that directly predicts run-up velocities for the present geometry and loading; a separate, explicit EurOtop run-up benchmark is presented as the fifth check below (Table 7). For the rip-rap baseline, characteristic flow velocities of the order of approximately 3–6 m/s are commonly reported for plunging-wave conditions in shallow water at the breaking depths typical of the study area (≈1.3 m, adopted screening value informed by HIDRONAV bulletin practice [19]). The CFD outputs fall within this indicative range at 53° and, at 60°, above it but within the same order of magnitude (Table 6), consistent with the relevant empirical literature at the screening level. This contrast is a comparative consistency check, not a hydraulic validation; the latter would require physical-model tests in a wave channel and dedicated van der Meer/EurOtop calculations.

Table 6. Order-of-magnitude check of CFD-predicted rip-rap run-up velocities against the empirical range derived from the van der Meer framework for plunging-wave conditions at the breaking depth of the study area.

Slope Angle (θ)	CFD Rip-Rap Range (m/s)	Empirical Expected Range (m/s) *	Interpretation
60°	6.71–8.38	≈3–6 (upper-bound case)	Same order of magnitude; above the indicative band
53°	3.35–5.03	≈3–6	Within empirical range
45°	<0.5–1.67	<3 (low-energy regime)	Consistent low-energy regime

* Indicative range only; not a case-specific empirical prediction. The 3–6 m/s figure was obtained as an order-of-magnitude reference compatible with characteristic flow velocities reported in armour-stability and run-up-related studies for plunging-wave conditions in shallow water [14,33,40]; it is not the result of a dedicated van der Meer calculation for the present case. Quantitative validation requires physical-model tests and dedicated empirical computations.

Fifth, an analytical benchmark against the EurOtop run-up framework [34] was added. The 2% exceedance run-up is estimated as $Ru2\%/Hm0 = \min(1.65 \cdot \gamma b \cdot \gamma f \cdot \gamma \beta \cdot \xi m - 1{,}0;\ \gamma f \cdot \gamma \beta \cdot (4.0 - 1.5/\sqrt{(\gamma b \cdot \xi m - 1{,}0)}))$, where $\xi m - 1{,}0 = \tan\alpha/\sqrt{(Hm0/Lm - 1{,}0)}$ is the breaker parameter and γb, γf, $\gamma \beta$ are the berm, roughness and obliquity influence factors (here $\gamma b = \gamma \beta = 1$). Wave inputs follow the site-specific risk study [21]: Hm0 = 2.0 m and Hmax = 3.5 m. The risk study indicates that peak-period data were extracted from the WWATCH III reanalysis used as wave input, but does not report the value adopted for the simulation [21]; the calculation was therefore performed parametrically for peak periods Tp = 12–16 s, representative of long-period anomalous swells on the Peruvian coast, with $Tm - 1,0 = Tp/1.1$. For the 53° slope ($\cot\alpha = 0.75$), the breaker parameter falls in the surging regime ($\xi m - 1,0 \approx 10$–17), so the second (maximum) branch of the formula governs. The formulation applied here is EurOtop's standard dike-slope branch; EurOtop 2018 [34] also provides a dedicated steep-slope formulation, which was not adopted because the benchmark is retained only as an indicative order-of-magnitude check, so the application of the standard branch to the present steeper slope is an extrapolation, and the comparison is indicative only. In addition, the estimates quoted for the maximum wave height apply the same formula, which is written in terms of the spectral significant wave height; this direct substitution is not part of the EurOtop formulation and is retained solely as an upper-bound proxy that adds conservatism to the indicative check. Likewise, Ru2% describes irregular-wave statistics, whereas the CFD simulates a single equivalent bore; agreement is assessed at the order-of-magnitude level, consistent with the screening scope of this study.

The results are summarised in Table 7. The estimated Ru2% is insensitive to the assumed period (7.2 m for Hm0 = 2.0 m and 12.3–12.5 m for Hmax = 3.5 m across Tp = 12–16 s), because the surging-branch maximum saturates for large $\xi m - 1,0$. The maximum free-surface elevations obtained from the CFD under the conservative 10 m/s scenario are consistent with this framework: the hollow-unit configuration reached 10.28 m at θ = 53° and 9.42 m at θ = 45°, i.e., between the Hm0-based and Hmax-based empirical estimates, while the rip-rap baseline exceeded the 10.4 m model crest at θ = 53°, in line with the Hmax-based estimate of 12.3–12.5 m, both referenced from the slope toe consistently with the definition of the defence height. The CFD outputs therefore fall within the same order of magnitude as the EurOtop framework for the site's design-wave heights. This supports the use of the CFD outputs as comparative indicators, while confirming that they are not a substitute for dedicated physical-model validation.

Table 7. Analytical benchmark of run-up indicators against EurOtop [34] for the 53° slope.

Case	Tp (s)	$\xi m - 1,0$	Ru2%—EurOtop (m)
Hm0 = 2.0 m (site Hs)	12/14/16	12.8/14.9/17.1	7.16/7.22/7.27
Hmax = 3.5 m (site max.)	12/14/16	9.7/11.3/12.9	12.31/12.44/12.54

A sensitivity analysis of the roughness parameters was also performed. Without the long-wave correction, the plausible γf range (0.40–1.00) spans run-up estimates of 2.9–7.2 m for Hm0 = 2.0 m; once the EurOtop correction for large breaker parameters is applied, all surfaces converge to the smooth-slope value (7.2 m), because $\xi m - 1,0 \geq 10$ for the entire plausible period range at this slope, and even for a short-period wind-sea case (Tp = 8 s, $\xi m - 1,0 \approx 8.5$), the corrected estimates differ by less than about 0.8 m across the full γf range. In other words, for the steep slope and long-period swell climate of the study site, the empirical framework itself indicates that classical surface roughness has a limited influence on extreme run-up. Two consequences follow. First, the run-up reductions observed in the CFD for the hollow-unit configuration should be attributed to the resolved interaction between the bore and the unit geometry (apparent flow deflection and momentum redistribution around the resolved geometry, not quantified through an energy budget), rather than to a roughness-coefficient effect, which is precisely why a geometry-resolving comparative CFD, rather than a γf-based calculation, was adopted as the discriminating tool. Second, the uncertainty introduced by the adopted γf range for the unit is bounded and does not alter the comparative conclusions of the study.

https://doi.org/10.3390/su18168201

2.11. Result Extraction and Technical-Performance Indicators

Time histories of centre-of-mass displacement, centre-of-mass velocity, angular velocity, and kinetic energy were extracted from the FEA using the SolidWorks time-response tool and exported to CSV files for further analysis in Excel and MATLAB (R2025a). From the CFD analysis, run-up velocity ranges and maximum free-surface elevations were extracted along the slope profile. The rigid-body kinetic-energy indicator of the unit (translational + rotational, Equation (3)) is computed in post-processing from the velocity fields obtained numerically by the FEA solver, using the standard rigid-body kinetic-energy decomposition into translational and rotational components:

$$T = 0.5\, m\, v_G^2 + 0.5\, I_G\, \omega^2 \tag{3}$$

where T is the rigid-body kinetic energy of the unit, m is the mass of the unit, v_G the velocity of the centre of mass, I_G the moment of inertia about the centre of mass, and ω the angular velocity [41]. This expression was used to quantify the residual kinetic energy after impact and its post-impact decay.

Five technical-performance indicators were defined for the comparison among designs: (i) residual kinetic-energy behaviour, evaluated from the post-impact kinetic-energy time history; (ii) maximum horizontal displacement of the centre of mass; (iii) qualitative structural-response screening, based on order-of-magnitude bounds of displacement, residual kinetic energy, and structural-response coherence under the adopted basal restraint; (iv) hydraulic performance indicators, expressed as run-up velocity range and maximum water-surface elevation along the slope; and (v) material reduction with respect to the control block. The first three indicators come from the FEA, the fourth from the CFD analysis, and the fifth from geometric quantification.

2.12. Circular-Economy and Embodied-Carbon Indicators

In addition to technical performance, circularity, material efficiency, and embodied-carbon indicators were defined with a functional unit of one block of 1 m^3 external volume. PET-waste valorisation was expressed as the mass of PET incorporated per block and, optionally, as an equivalent number of 3 L bottles. Material efficiency, by geometric design, was expressed as the ratio between effective material volume and external block volume. A preliminary cradle-to-gate embodied-carbon estimate was calculated using the reference Global Warming Potential (GWP) factors described in Section 3.7 [20,42,43]. Reuse and end-of-life considerations were treated qualitatively as future design and life-cycle assessment considerations rather than as quantified indicators in the present study. Additional numerical parameters and supporting results are provided in the Supplementary Materials.

3. Results

The numerical results are presented in two complementary parts: the FEA tracks comparative structural-response trends of the proposed unit and control configuration under the equivalent impact load, while the CFD compares the hydraulic behaviour of the hollow PET–concrete configuration with the rip-rap baseline. The conservative reference velocity of 10 m/s and a model slope height H = 10.4 m were considered for three slope inclination angles (θ = 60°, 53°, and 45°); the site-referenced velocity scenarios (3, 5 and 7 m/s at θ = 53°, Section 2.6) are reported in Section 3.5. The results presented below correspond to the adopted evaluation scheme and must be interpreted within the simplified assumptions of the model.

3.1. Simulation Case 1: Slope with θ = 60°

Figure 4a shows the results for the rip-rap configuration. Under these conditions, the simulated water surface exceeded the 10.4 m defence height, generating overtopping with run-up velocities ranging from 6.71 to 8.38 m/s.

In contrast, under the same boundary conditions, the configuration with hollow PET–concrete units (Figure 4b) showed a reduction in flow velocity, with simulated values in the range of 2.66 to 4.00 m/s. Nevertheless, the simulated water surface still exceeded the 10.4 m defence height.

3.2. Simulation Case 2: Slope with θ = 53°

In the rip-rap configuration (Figure 4c), the simulated water surface again exceeded the 10.4 m defence height, with run-up velocities between 3.35 and 5.03 m/s.

For the slope with hollow PET–concrete units (Figure 4d), the simulated run-up velocity decreased to a range of 1.33 to 2.66 m/s, and the maximum height reached by the water surface was 10.28 m. This value lies below the crest level of the coastal defence (H = 10.4 m), with a small margin of 0.12 m.

3.3. Simulation Case 3: Slope with θ = 45°

In the rip-rap configuration (Figure 4e), the flow reached the defence crest level (H = 10.4 m), with extracted run-up velocities extending from below the 0.5 m/s extraction threshold to 1.67 m/s.

The configuration with hollow PET–concrete units (Figure 4f) showed the best relative performance among the simulated cases. The maximum flow elevation was 9.42 m; the simulated free surface remained below the model crest under the adopted assumptions.

3.4. Comparative Synthesis

Table 8 summarises the results obtained for the three slope configurations evaluated.

Table 8. Comparison of flow run-up velocities and run-up heights for slopes with rip-rap and with hollow PET–concrete units.

Slope Angle (°)	Rip-Rap Velocity Range (m/s)	Hollow-Unit Velocity Range (m/s)	Max. Flow Height with Hollow PET–Concrete Units (m)	Overtopping with Hollow PET–Concrete Units
60	6.71–8.38	2.66–4.00	>12	Yes
53	3.35–5.03	1.33–2.66	10.28	No
45	<0.5–1.67	<0.5 *	9.42	No

* For the 45° case, the notation < 0.5 denotes extracted run-up velocities below the post-processing extraction threshold of 0.5 m/s used in this study; the lower bound of the rip-rap range is likewise below this threshold. Below-threshold values are not numerically resolved and are therefore reported relative to the threshold rather than as physical zeros, to avoid spurious resolution of near-zero numerical noise. The threshold was selected to filter the near-zero numerical noise of the solver in the quiescent region behind the armour. The comparative conclusion is robust to this choice because it rests on the large separation between the two configurations (the hollow-unit run-up velocities are several times lower than the rip-rap values across the whole range, Table 8) rather than on the near-zero values filtered by the threshold: shifting the cut-off between 0.2 and 0.8 m/s reclassifies only the lowest-velocity cells of the quiescent region and does not alter the ordering between configurations.

Comparing the midpoints of the run-up velocity ranges in Table 8 against the rip-rap baseline, the hollow PET–concrete configuration suggests reductions of approximately 56% for θ = 60° (from a midpoint of 7.55 m/s to 3.33 m/s) and 52% for θ = 53° (from 4.19 m/s to 2.00 m/s). For the 45° case, the rip-rap baseline already shows very low run-up velocities (<0.5–1.67 m/s, relative to the post-processing extraction threshold); the resulting percentage reduction for this case should therefore not be interpreted as a meaningful comparative metric and is not reported, since both armour conditions operate close to the numerical noise floor of the extraction protocol. Restricting the comparison to the configurations with significant flow energy in both armour conditions (60° and 53°), the average run-up velocity reduction is (56% + 52%)/2 ≈ 54%. The percentage reduction was computed as $\Delta v = (vmid,RR - vmid,HC)/vmid,RR \times 100$, where vmid,RR and vmid,HC are the midpoint velocities for rip-rap and hollow PET–concrete configurations, respectively. The hydrodynamic context that supports this comparison is illustrated in Figure 5, which shows the wave-breaking conditions at the reference depth of 1.3 m adopted for the Chucuito–Callao study area (screening value informed by HIDRONAV bulletin practice [19]).

In addition to the CFD-based hydraulic indicators, the companion FEA was used to track structural-response trends of the hollow PET–concrete unit at each slope-base angle, under the same equivalent impact load. The FEA component is used here as a qualitative structural-response screening tool that complements the hydraulic indicators by indicating consistent structural-response trends across configurations under the adopted basal restraint; absolute stress, displacement, and factor-of-safety values are not reported, as the equivalent loading scheme is not site-specific. The residual kinetic energy used as an ordinal indicator in this screening is the rigid-body decomposition reported in Equation (3). The ordinal screening is summarised in Table 9.

Table 9. Qualitative structural-response screening of the hollow PET–concrete unit under the equivalent impact load defined in Section 2.6. Results are expressed as ordinal comparisons within the simulation set and do not constitute structural-design verification.

Slope Angle	Relative Displacement	Relative Residual Kinetic Energy	Structural-Response Outcome	Interpretation
60°	Highest among cases	Highest among cases	No adverse trend	Geometry alone insufficient at this angle; complementary system-level measures required
53°	Intermediate	Intermediate	No adverse trend	Adequate structural-response trend within the simulation set
45°	Lowest among cases	Lowest among cases	No adverse trend	Most favourable structural-response trend within the simulation set
Control	Reference	Reference	No adverse trend	Reference configuration

Note. The structural-response screening is based on relative displacement and residual kinetic-energy trends under the adopted basal restraint. The FEA does not evaluate material failure, PET–matrix interface failure, overturning, or basal separation and does not constitute structural-design verification.

No adverse displacement or residual-energy trend was observed for the hollow PET–concrete unit under the adopted equivalent loading condition and basal restraint. The scope limits of this restrained-base screening are stated in Section 2.8.

3.5. Velocity-Sensitivity Analysis at $\theta = 53°$

To address the dependence of the results on the single conservative velocity, six additional CFD runs were performed at $\theta = 53°$ (hollow unit and rip-rap baseline at inlet velocities of 3, 5 and 7 m/s, Section 2.6), together with the corresponding FEA transient analyses with loads recalculated via Equation (1). The 5 m/s case corresponds to the maximum flow velocity of the site-specific Delft3D inundation model [21], while 3 and 7 m/s bracket it (Table 10).

Table 10. Hydrodynamic velocity-sensitivity results at θ = 53° from the CFD analysis. Run-up velocities are profile-scale readings from the converged velocity-field cut-plots; maximum free-surface elevations are derived trigonometrically from the run-up length along the slope. The associated design impact loads (Equation (1)) are listed for reference. The 10 m/s row originates from the conservative angle-comparison run set computed on the earlier, coarser mesh family (Section 2.9); quantitative comparison between that row and the 3–7 m/s sensitivity series is not intended.

Inlet Velocity (m/s)	Peak Load F, Equation (1) (kN)	Rip-Rap: Run-Up Velocity (m/s)	Hollow Unit: Run-Up Velocity (m/s)	Velocity Reduction, Midpoint (%)	Hollow Unit: Max. Elevation (m) *
3	41.5	2.72–3.00	0.81–1.63	≈57.3	7.77
5	115.3	2.72–3.63	0.90–1.81	≈57.3	9.36
7	226.0	3.18–4.45	1.90–3.81	≈25.2 †	10.98
10 (cons.)	461.3	3.35–5.03	1.33–2.66	≈52.4	10.28

* In all three new cases, the rip-rap free surface exceeded the crest level (H = 10.4 m, consistent with the reference dimensions of Figure 2). † At 7 m/s, the midpoint reduction falls to approximately 25%, and the rip-rap and hollow-unit velocity ranges overlap substantially, so the comparative advantage becomes less robust than at the lower velocities. The structural response of the unit under these load levels is addressed in ordinal terms in the following paragraph and in Table 9, consistently with the screening scope of the FEA component; absolute displacement or stress values are not reported, as the equivalent loading scheme is not site-specific.

The flow-trajectory visualisations of the six runs are shown in Figure 6. Under the site-referenced scenarios, the hollow unit maintained run-up velocity reductions of approximately 57% at 3 and 5 m/s (midpoint criterion), slightly above the 52–56% obtained under the conservative 10 m/s scenario, while the rip-rap baseline exceeded the reported crest level in all three cases. At 7 m/s, however, the midpoint reduction fell to approximately 25%, and the rip-rap and hollow-unit velocity ranges overlapped substantially, so the comparative advantage became less robust; in addition, the maximum free-surface elevation of the hollow-unit configuration (10.98 m) exceeded the 10.4 m crest. The protective benefit of the unit is therefore confined to the site-referenced loading range: at the site-modelled maximum of 5 m/s and below, the unit suppresses overtopping with margins of 2.6 and 1.0 m and maintains midpoint velocity reductions of ≈57%, whereas at 40% above that maximum (7 m/s) the midpoint reduction falls to ≈25% with overlapping ranges and the unit no longer prevents overtopping in the simulation. Relative to this series, the larger midpoint reduction (≈52%) and lower maximum elevation (10.28 m) obtained at 10 m/s should not be read as a physical recovery of the comparative advantage beyond 7 m/s: the 10 m/s case belongs to the conservative angle-comparison run set computed on the coarser mesh family (Section 2.9), and quantitative cross-set comparison is not intended (Table 10). The corresponding FEA transient analyses used the recalculated peak loads of 41.5, 115.3 and 226.0 kN for the 3, 5 and 7 m/s scenarios, respectively, following Equation (1). Consistent with the ordinal structural-response screening adopted in this study (Table 9), these additional FEA cases were interpreted comparatively; their absolute transient displacement and residual kinetic-energy values are not reported numerically here. This bounds the applicability of the concept and reinforces the need for wave-flume validation at the upper end of the loading range. The maximum elevations of the new runs (7.77–10.98 m) lie within or below the EurOtop-based empirical band of Table 7 (7.2 m for Hm0 and 12.3–12.5 m for Hmax), reinforcing the order-of-magnitude consistency of the CFD outputs.

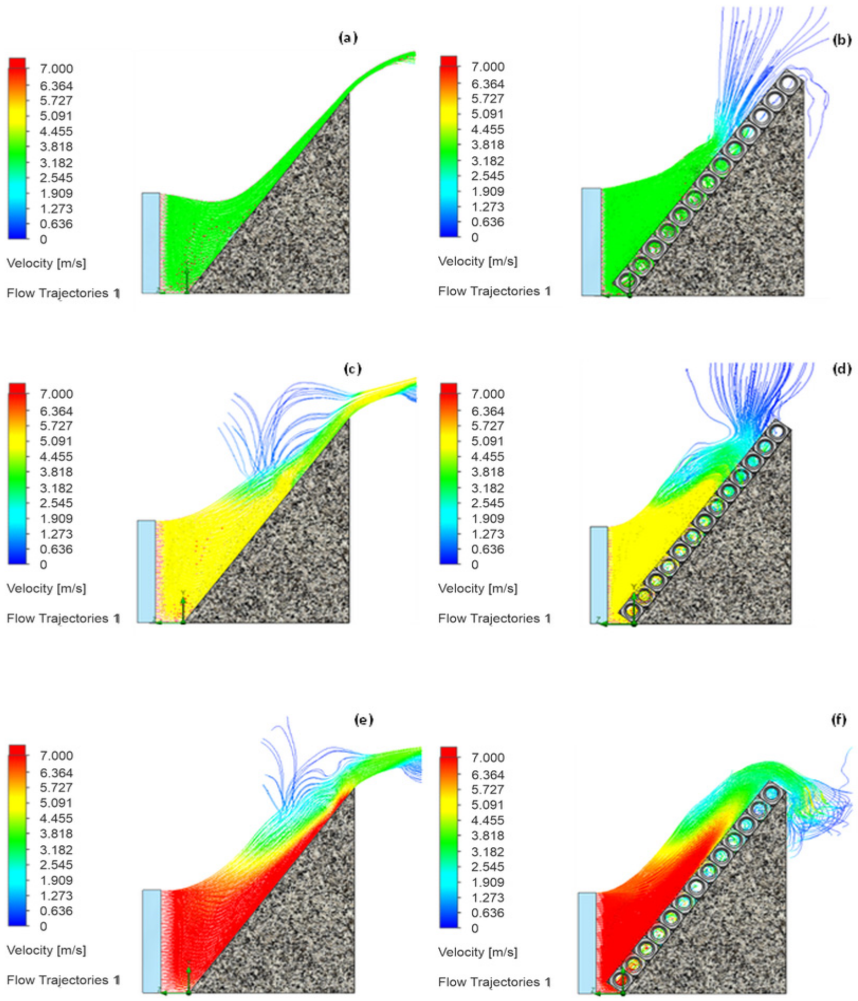

Figure 6. Flow-trajectory visualisations of the velocity-sensitivity runs at θ = 53°, with a common colour scale (0–7 m/s) across all panels: (**a**) rip-rap and (**b**) hollow PET–concrete unit at 3 m/s; (**c**) rip-rap and (**d**) hollow PET–concrete unit at 5 m/s; (**e**) rip-rap and (**f**) hollow PET–concrete unit at 7 m/s. The common scale makes a given colour correspond to the same velocity in every panel, allowing direct visual comparison between configurations and inlet velocities. Low-velocity trajectory traces visible above the crest in some panels are elements of the trajectory visualisation; the maximum free-surface elevations reported in Table 10 were extracted from velocity-field cut-plots (Section 2.11).

3.6. Circular-Economy Analysis and Material Efficiency

From a circular-economy perspective, the hollow geometry implies a substantial reduction in material consumption. A solid concrete cube with the same external footprint would have an effective volume of 0.989 m^3, with the small remainder relative to the 1 m^3 external envelope corresponding to the chamfered edges. The hollow PET–concrete unit requires only 0.380 m^3 of composite, which corresponds to about 38% of the equivalent solid-block volume and therefore implies a material saving of approximately 62% per functional unit relative to a solid block of equivalent footprint. This material saving is the key geometric contribution to the sustainability metrics reported in Section 3.7.

The waste-valorisation potential was quantified at the 10% PET volumetric dosage adopted in Section 2.3. The PET volume per unit is therefore $0.10 \times 0.380 = 0.038$ m^3. Adopting a representative density of 1335 kg/m^3 for the recycled-PET fraction (note: this is the density of the PET phase itself; the consolidated PET–concrete composite has a density of approximately 2250 kg/m^3, see Table 1), the PET mass per unit is $m_{PET} = 0.038 \times 1335 \approx 50.7$ kg. Taking 64 g as the average mass of a 3 L post-consumer PET bottle (an upper-bound estimate for thick-walled water-bottle formats), the equivalent number of bottles per unit is $N_{bottles} = 50.7/0.064 \approx 793$ bottles (Figure 7). For lighter bottle formats (≈50 g), the equivalent count rises to about 1015 bottles. These figures should be read as representative of bottle-equivalent valorisation rather than as a strict count, as actual mass per bottle varies with brand, format, and post-consumer condition.

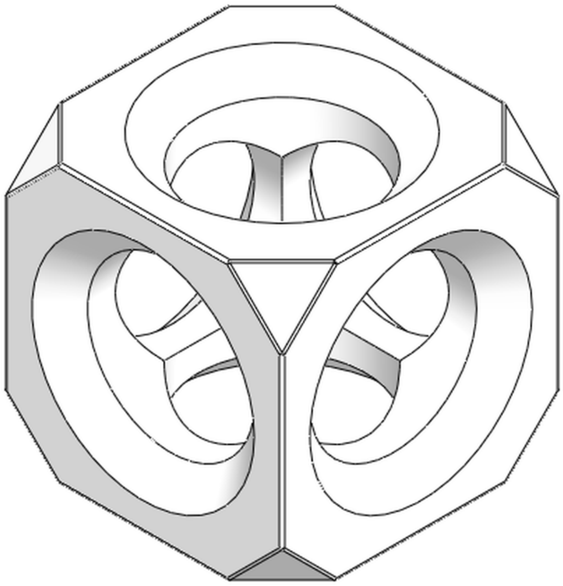

Figure 7. Isometric view of the proposed hollow PET–concrete modular unit. External dimensions: 1 m × 1 m × 1 m cube (1 m^3 external volume); hollow multi-opening geometry incorporating nominal 0.60 m circular openings connected through an internal void. The hollow geometry uses approximately 38% of the equivalent solid-block volume (≈62% material saving per unit) and enables the valorisation of approximately 793 post-consumer 3 L PET bottles per unit at a 10% volumetric PET dosage.

3.7. Preliminary Cradle-to-Gate Embodied-Carbon Assessment

To complement the material-saving and waste-valorisation indicators with a sustainability-oriented metric, a simplified cradle-to-gate embodied-carbon assessment was performed for the functional unit, defined as one modular unit of 1 m^3 external volume. The system boundary covers Modules A1–A3 of EN 15804: raw-material extraction and processing, transport to plant, and manufacture of the unit. Modules A4–A5 (transport to site and installation), B1–B7 (use, maintenance, repair, replacement), and C1–C4 (end of life) are not included in this preliminary estimate. The figures are not equivalent to a full cradle-to-grave LCA and should not be read as such. It should also be stressed that the hydraulic indicators reported in Sections 3.1–3.4 are system/profile-level (run-up velocity and water-surface elevation along a slope cross-section), whereas the material and embodied-carbon indicators reported here are unit-level (per modular unit). A complete like-for-like comparison with rip-rap would require a functional unit defined per linear metre of protected coastline at an equivalent protection level; this is identified as a limitation of the present assessment (Section 4.8).

Three reference scenarios were considered: (a) solid conventional block (control), modelled as 0.989 m^3 of ready-mixed concrete; (b) hollow conventional block, with the same hollow geometry as the proposed unit but fabricated entirely with ready-mixed concrete (0.380 m^3); and (c) hollow PET–concrete block (proposed), with 0.342 m^3 of cementitious matrix and 0.038 m^3 of recycled-PET fraction (≈51 kg). Reference Global Warming Potential (GWP) factors were adopted as order-of-magnitude screening values informed by peer-reviewed LCA studies: approximately 260–350 kg CO_2-eq per m^3 of ready-mixed concrete across typical mix designs [42,43] and of the order of 1 kg CO_2-eq per kg for mechanically recycled PET [20]. The central case adopted 325 kg CO_2-eq/m^3 for concrete and a rounded central screening value of 1.0 kg CO_2-eq/kg for recycled PET; the boundary values were used for the sensitivity analysis. All emission factors and empirical references used in this assessment, including the GWP factors above and the van der Meer-related ranges in Section 2.10, were adopted as order-of-magnitude inputs for screening-level comparison, not as site-specific design values. The central-case results are summarised in Table 11.

Table 11. Preliminary cradle-to-gate embodied-CO_2 estimate per functional unit, central-case factors (325 kg CO_2-eq/m^3 concrete; 1.0 kg CO_2-eq/kg recycled PET).

Scenario	Concrete Vol. (m^3)	PET Mass (kg)	Embodied CO_2 (kg CO_2-eq)	Reduction vs. Solid
(a) Solid conventional block	0.989	0	≈321	—
(b) Hollow conventional block	0.380	0	≈124	−61%
(c) Hollow PET–concrete (proposed)	0.342 *	≈51	≈162 **	−50%

* The 0.380 m^3 of composite includes 90% cementitious matrix and 10% recycled-PET fraction by volume; the cementitious-matrix volume is therefore 0.342 m^3. ** Estimated as $0.342 \times 325 + 51 \times 1.0 \approx 162$ kg CO_2-eq per unit.

Three readings emerge from Table 11. First, a substantial fraction of the embodied-CO_2 reduction comes from the hollow geometry itself: even fabricated with conventional concrete, the hollow block reduces embodied CO_2 by ≈ 61% relative to the solid control. The principal carbon benefit is therefore driven by the geometry, not by the recycled-PET fraction. Second, when the cementitious matrix is partially substituted with recycled PET, the unit retains a substantial reduction (≈50%) relative to the solid control, but exhibits a slightly higher embodied CO_2 than the all-concrete hollow block (≈162 vs. ≈124 kg CO_2-eq) under this conservative cradle-to-gate accounting because the 1.0 kg CO_2-eq/kg factor for recycled PET is added to the cementitious-matrix burden. Under different assumptions for the recycled-PET supply chain, the recycled-PET option could fall above or below the all-concrete hollow option. Third, no credits for avoided landfill or avoided incineration of post-consumer PET were applied in this estimate; including such credits, through a cradle-to-grave LCA with end-of-life modelling, would shift the comparison in favour of the recycled-PET option but would also require characterising the displaced waste-management baseline, which is beyond the present scope. Until such a full LCA is carried out, the recycled-PET fraction should be reported primarily for its plastic-waste valorisation co-benefit, while the embodied-CO_2 reduction is attributed to the hollow geometry.

To assess the robustness of these figures, a sensitivity analysis was performed by varying the concrete GWP factor by ±20% and the recycled-PET GWP factor by ±50% around their central values. Table 12 summarises the results.

Table 12. Sensitivity analysis of the embodied-CO_2 reduction (Scenario c vs. a) under variations of the central emission factors.

Scenario Varied	GWP Concrete (kg CO_2-eq/m^3)	GWP Recycled PET (kg CO_2-eq/kg)	Embodied CO_2 Proposed Unit (kg CO_2-eq)	Reduction vs. Solid
Central case	325	1.0	≈162	−50%
Low concrete factor (−20%)	260	1.0	≈140	−46%
High concrete factor (+20%)	390	1.0	≈184	−52%
Low PET factor (−50%)	325	0.5	≈137	−58%
High PET factor (+50%)	325	1.5	≈188	−42%

Across the explored range, the estimated reduction in embodied CO_2 for the proposed unit relative to the solid control remains within approximately 42–58%. This range supports the qualitative ranking among scenarios but should not be taken as a definitive figure: local cement clinker content, supplementary cementitious materials, transport distances, regional electricity mix, and the actual recycled-PET supply chain could shift absolute values further. A full cradle-to-grave LCA, incorporating site transport, installation, marine-environment service life, maintenance, and end-of-life scenarios, remains a priority for subsequent work [20,42–44]. Until that assessment is completed, the embodied-CO_2 figures reported here should be read as preliminary, order-of-magnitude estimates intended to size the potential sustainability benefit of the proposed unit, not as a verified low-carbon claim.

4. Discussion

This section discusses the simulation findings, places them in context with relevant literature on coastal armour stability and recycled-PET concrete, makes the sustainability implications of the proposal explicit, and outlines limitations, environmental risks, and a research roadmap. Throughout, results are framed as preliminary numerical evidence rather than as a validated coastal-defence solution.

4.1. Hydraulic Findings and Their Interpretation

The simulation results reported in Section 3.4 indicate consistent run-up velocity reductions for the hollow PET–concrete configuration relative to the rip-rap baseline at both energetic slope angles evaluated (60° and 53°). Under the adopted assumptions (smooth-surface CFD with roughness assessed analytically, and no resolution of flow within and between individual units), in the 10 m/s angle-comparison runs reported in Section 3.4, the simulated free surface of the hollow-unit configuration did not exceed the model crest (H = 10.4 m) at θ = 53° and 45°. This statement is conditional on those assumptions and on the model geometry; it is not an overtopping verification of the actual Chucuito defence, whose crest elevations are substantially lower (terrain largely below ≈4 m a.s.l., with site-modelled inundation depths of up to 4 m [21]). These outcomes are consistent with the well-established role of armour-unit geometry, porosity, and surface roughness in dissipating incident wave energy on rubble-mound structures [13,14,33,40]. The CFD output for the rip-rap baseline shows the same order of magnitude as indicative ranges from the van der Meer armour-stability and run-up-related framework for plunging-wave conditions at the same breaking depth (Table 6, Section 2.10); this consistency check supports the use of these CFD outputs as comparative indicators only, not as definitive hydraulic-design quantities.

The CFD idealises both configurations with hydraulically smooth surfaces while explicitly resolving the module geometry (Section 2.9); therefore, the additional run-up reduction attributed here to the hollow PET–concrete units, above the rip-rap baseline, reflects the resolved interaction between the bore and the unit geometry rather than a prescribed roughness effect. This attribution is consistent with the analytical benchmark of Section 2.10, which indicates that, for the steep slope and long-period swell climate of the site, classical roughness-coefficient effects on extreme run-up are limited ($\xi m - 1{,}0 \geq 10$), while pore- and gap-scale flow within the armour layer remains unresolved. The reported velocity reductions are contingent on the adopted equivalent loading scheme, solver assumptions, cross-sectional flow representation, RANS k–ε closure, and smooth-surface idealisation. They are relative indicators within the common numerical environment and should not be transferred directly to irregular field-wave conditions; physical-model testing under irregular waves, oblique incidence and varying breaking conditions is required to confirm their magnitude. The structural-response screening reported in Table 9 indicates that the simulated hydraulic improvements were not achieved at the expense of structural-response coherence under the adopted loading assumptions and basal restraint, as no adverse displacement or residual-energy trend was observed for the hollow PET–concrete unit across the three slope angles; resistance to overturning and basal separation lies outside this restrained-base screening (Section 2.8) and remains part of the validation roadmap (Section 4.9). It is also relevant to acknowledge that rip-rap is not the only baseline against which an emergent modular unit could be benchmarked: established artificial armour units (e.g., Tetrapods, Accropode, Xbloc, Core-Loc) provide an alternative reference that explicitly internalises interlocking and porosity effects, and Nature-based Solutions (NbS) or Ecosystem-based Adaptation (EbA) approaches offer a complementary class of coastal-protection strategies whose comparative performance and co-benefits differ structurally from those of hard-armour solutions. However, Tetrapods, Accropode, Xbloc and Core-Loc are proprietary, geometrically optimised precast units whose embodied material and carbon profiles differ substantially from both rip-rap and the present hollow unit; a fair circularity and carbon comparison against them would require a dedicated life-cycle inventory for each system, which is beyond the screening-level scope of this study. Rip-rap, by contrast, shares a comparable order of material complexity with the proposed unit and is the dominant coastal-defence practice in the Peruvian context, which is why it was retained as the hydraulic baseline for the comparative CFD assessment. The material-efficiency, circularity and embodied-carbon indicators are instead evaluated per modular unit against the solid-concrete and hollow-concrete block references defined in Section 3.7, rather than against rip-rap. A like-for-like system-level carbon comparison with rip-rap would require a functional unit based on an equivalent level of coastal protection, for example, per linear metre of protected coastline; extending the comparative scope in that direction is identified as a follow-up step (Section 4.9).

4.2. Material Efficiency and Plastic-Waste Valorisation

The hollow geometry uses approximately 38% of the equivalent solid-block volume, implying a material saving of about 62% per functional unit relative to a solid block of equivalent footprint. This is the dominant geometric driver of the sustainability metrics reported in Section 3.7. The partial substitution of cementitious matrix with recycled PET adds a tangible plastic-waste valorisation co-benefit at the 10% PET dosage adopted ($\approx$51 kg PET per unit, equivalent to $\approx$793 post-consumer 3 L bottles based on a 64 g per-bottle average; $\approx$1015 bottles for lighter 50 g formats).

These figures should not be interpreted as a proportional reduction in total carbon footprint without further analysis: the 62% volumetric saving applies to material consumed, not to embodied CO_2, which is governed by the specific GWP factors of concrete and recycled PET. The cradle-to-gate estimate in Section 3.7 quantifies this distinction and shows that the proposed unit reduces embodied CO_2 by $\approx$ 50% (sensitivity range 42–58%) relative to a solid concrete reference. It is important to stress that this embodied-carbon benefit is primarily driven by the hollow geometry, not by the recycled-PET fraction itself; the recycled-PET fraction may, depending on the assumed GWP factor and on whether end-of-life credits are included, slightly improve or slightly worsen the embodied-CO_2 score relative to an all-concrete hollow baseline. Its principal sustainability contribution is therefore the plastic-waste valorisation co-benefit rather than an intrinsic embodied-CO_2 reduction.

4.3. Differential Performance with Slope Angle

The angular dependence of the simulated response indicates that the proposed unit is most effective within the best-performing range of the tested slope configurations, i.e., slope angles in the approximate range of $45^\circ \leq \theta \leq 53^\circ$. For clarity, these are termed "steep-to-moderate, footprint-constrained" slopes throughout this manuscript, a study-specific label rather than a conventional coastal-engineering category, since they are markedly steeper than the gently sloping armour configurations (typically 1V:1.5H to 1V:3H, i.e., $\approx$18–34°) commonly adopted in conventional rubble-mound coastal-engineering practice. The steeper geometries explored here reflect the constrained vertical-edge condition of the Chucuito–Callao coastal setting, where landward space is limited by existing urban infrastructure. At $\theta = 60°$, the simulated flow still surpasses the crest, so the geometry alone would be insufficient and would require complementary measures (greater freeboard, berms, or adjusted defence height) for that loading scenario. At $\theta = 45°$, the simulated performance is slightly better than at 53°, but the marginal gain over 53° is small, suggesting an asymptotic regime within the explored slope range. This pattern is consistent with established energy-dissipation behaviour of rubble-mound armour layers, where slope, equivalent roughness, and porosity interact non-linearly to determine run-up [13–15,40]. Extension of the framework to gentler slopes more representative of conventional coastal-engineering practice is identified as a follow-up step (Section 4.9).

4.4. Sustainability Implications for Coastal Infrastructure

The combined indicators, material saving, plastic-waste valorisation, and embodied-CO_2 reduction, position the proposal at the intersection of three sustainability dimensions relevant to coastal infrastructure. First, the unit can absorb post-consumer PET volumes that, in vulnerable coastal contexts such as Lima–Callao, currently face limited valorisation rates [6]; this contributes directly to circular-economy and waste-management targets (SDG 12) [7,8,45] and aligns with the policy direction of Peru's General Solid Waste Management Law (Legislative Decree 1278) [46] and Law 30884 on the regulation of single-use plastics [47]. Second, by reducing both the cementitious-matrix volume per unit and the embodied CO_2 per unit, the proposal aligns with low-carbon infrastructure trajectories increasingly required of coastal-adaptation works (SDG 13). Third, by providing a proposed surface-protection response relevant to slope stabilisation in a sector exposed to wave action and shoreline retreat, the proposal contributes to resilient and inclusive urban infrastructure (SDG 11).

The trade-off among these dimensions is not trivial. A higher PET dosage would increase plastic valorisation but might reduce mechanical strength and durability beyond acceptable thresholds [9,11,20,48]. A larger hollow cavity would amplify material saving but might compromise the structural response under impact loading. Steeper slopes save lateral footprint but lose hydraulic effectiveness. Decisions on dosage, geometry, and slope therefore depend on the specific weighting of hydraulic performance, durability, material efficiency, and embodied carbon under local conditions, a multi-criteria optimisation that is beyond the scope of this preliminary study but constitutes a natural follow-up.

4.5. Environmental Risks Associated with PET in Marine Use

The presence of polymeric material in a marine-exposed cementitious matrix introduces specific environmental considerations that must be acknowledged and managed in any field application. The risk profile depends critically on whether the PET fraction remains encapsulated within an intact cementitious matrix or becomes exposed at the surface through abrasion, cracking, or progressive matrix wear; the dosage, granulometry, and quality of the PET–matrix bond, together with the severity of marine exposure, are the main controlling variables [9,11,20,48,49].

Three concerns are particularly relevant when the PET fraction becomes exposed. First, photodegradation of exposed PET by UV radiation, combined with abrasion by suspended sediments and wetting–drying cycles, can lead to surface fragmentation and microplastic release over the service life [9,20,48,49]. Second, leaching of additives or oligomers from the recycled-PET fraction into the marine environment, although typically limited for PET relative to other polymers, has not been characterised for the specific composite and exposure conditions of this proposal. Third, hydrolytic degradation under prolonged immersion can affect long-term mechanical performance and the integrity of the PET–matrix interface, potentially accelerating the transition from encapsulated to exposed PET. These polymer-specific concerns interact with established marine-durability mechanisms of cementitious materials (chloride and sulphate ingress, wetting–drying and freeze–thaw cycling, abrasion under suspended-sediment load, biofouling, and fatigue under cyclic wave loading) that progressively damage the matrix, the PET–cement interface, and ultimately the unit's structural performance. Marine-durability assessment of the composite must therefore address both the polymer- and the matrix-side mechanisms together; their combined evolution determines the rate at which encapsulation is lost and structural degradation accumulates.

Although the present study does not include dedicated leachate or durability tests, the published experimental literature on PET-incorporated concrete provides quantitative benchmarks against which the expected envelope of behaviour for the proposed composite can be bounded. Using a modified Toxicity Characteristic Leaching Procedure (TCLP) on concrete specimens cured for 28 days with PET aggregate replacing 10–40% of the natural coarse aggregate, Sau, Shiuly and Hazra [50] reported no detectable microplastic in the leachate across the full PET replacement range (PET10 to PET40), while polyethylene (PE)-based and mixed PET–PE specimens released detectable microplastics under the same protocol. The same study reported rapid chloride penetration (RCPT) of 435–635 Coulombs for PET-incorporated concrete compared with 678 Coulombs for the control mix, indicating a 6–36% reduction in chloride-ion penetrability when PET is incorporated. Saxena et al. [51] independently reported substantial increases in impact-energy absorption relative to the control mix for PET replacements up to 20%. These figures should not be transferred directly to the proposed coastal unit since they were obtained for terrestrial concrete formulations and for relatively short curing periods (28 days) and they do not address long-term UV photodegradation, biofouling, or cyclic wave loading. They do, however, indicate that within the limits of the published experimental envelope, the dominant microplastic risk for PET-incorporated cementitious composites originates from polymer types other than PET (notably PE) and from loss of matrix integrity, rather than from the PET aggregate itself when it remains encapsulated. This benchmark supports the screening-level framing of the present study but does not substitute for the dedicated marine-exposure tests identified at the end of this section.

In the proposed unit, the PET fraction is intended to remain encapsulated within the cementitious matrix, which is expected to limit direct exposure of the polymer surface to the marine environment relative to free PET. This expectation, however, holds only as long as the matrix remains free of cracking, abrasion-induced loss of cover, and matrix degradation; encapsulation cannot be claimed as inherently safe in the absence of empirical evidence. Loss of structural integrity may accelerate PET exposure and the associated environmental risks, since cracking, spalling, or surface wear progressively transition encapsulated PET into exposed PET and increase the surface area available for photodegradation, abrasion, and hydrolysis. The 10% volumetric PET dosage adopted here is a working value taken from prior tests on terrestrial applications [9,11]; it should not be assumed optimal for marine exposure. Standardized characterisation is therefore required before any pilot deployment, including: (i) accelerated abrasion testing under simulated sediment-laden flow; (ii) leachate testing of additives and oligomers under representative seawater conditions; (iii) accelerated ageing combining wetting–drying, sulphate, chloride, and UV exposure; (iv) microplastic-release monitoring at the unit surface and in the surrounding water under cyclic loading; and (v) dosage-optimization tests in the 5–20% PET range. These tests are listed as a priority research line in Section 4.9. Taken together, the encapsulation-dependent risk profile identified above indicates that maintaining matrix integrity, through adequate cover thickness, crack control, and quality-controlled casting, is the primary lever for limiting microplastic release from this composite and should be prioritised in design and quality assurance ahead of reducing the PET dosage itself.

4.6. Durability, Implementation and Cost-Related Considerations Relative to Conventional Structures

A meaningful comparison with conventional coastal-protection structures must consider service life, maintenance and marine-exposure durability in addition to hydraulic performance. Conventional rock armour (rip-rap) is characterised by long service lives governed mainly by armour-stone displacement and abrasion, with maintenance consisting of periodic re-profiling and stone replacement [13]. Conventional concrete armour units offer engineered hydraulic behaviour but concentrate embodied carbon and require quality-controlled casting [14–16]. For the proposed PET–concrete unit, the durability question is dominated by the long-term behaviour of the composite under marine exposure, whose mechanisms and published experimental envelope are examined in Section 4.5; no marine-exposure dataset exists for the specific 10/90 mix and hollow geometry proposed here, and durability performance therefore cannot yet be claimed, only bounded by analogy; experimental evidence of degradation of recycled PET fibres in Portland-cement environments [52] reinforces the need for mix-specific marine-exposure testing. This is why marine-durability characterisation is placed early in the validation roadmap (Section 4.9). Regarding implementation, the unit is potentially compatible with precast-concrete manufacturing, subject to mould design and casting trials. Its placement may be compatible with equipment used for standard modular revetments, subject to dedicated handling and installation assessment. The implications of the hollow geometry for unit weight, transport and installation should be quantified in subsequent implementation studies.

A full economic analysis is beyond the scope of this preliminary study, and no claim of economic viability is made here. Any rigorous comparison must be performed on a whole-life-cost basis, not on capital expenditure (CAPEX) alone, because durability, maintenance frequency, and end-of-life management may differ substantially between the proposed unit and rip-rap. The proposed unit involves higher per-element costs than quarried rip-rap because it is a precast, formworked element; this difference may, in principle, be partially offset by lower per-unit material consumption, modular handling and installation, and localised maintenance enabled by modularity, but the magnitude of this offset cannot be quantified from the information available in the present study. A dedicated whole-life-cost analysis should be performed per linear metre of protected coastline (rather than per unit) and should cover raw materials, precasting (mould fabrication and amortisation, curing, quality control), transport, installation, inspection and maintenance, partial replacement after storm events, and end-of-life management. The recycled-PET fraction can be sourced through existing post-consumer collection chains in Lima–Callao [6,45]; this local sourcing route is expected to be the main lever for narrowing any cost gap with rip-rap and is prioritised in the whole-life-cost analysis identified in Section 4.9.

4.7. Practical Implications

The implications discussed below are intended for controlled pilot deployment, not as direct recommendations for site implementation. Any application beyond a research stage pilot would require, as a minimum precondition, completion of hydraulic, durability, environmental release, and economic validation of the unit. Within these limits, the proposal is potentially relevant to four user groups. Coastal municipalities and adaptation agencies could consider it for monitored pilot projects on moderate-slope sectors with documented PET-waste pressure and where replacement of failed conventional armour is needed. Coastal infrastructure designers could use the framework presented here as a comparative baseline when assessing modular armour alternatives that combine geometric efficiency and recycled material valorisation. Solid-waste managers could explore the unit as a placement route for post-consumer PET volumes that currently lack high-value valorisation pathways. Precast concrete plants could use the unit as a candidate product line, given its compatibility with existing manufacturing infrastructure.

Conditions under which the unit appears most relevant include steep-to-moderate, footprint-constrained slopes within the tested 45–53° range (Section 4.3), local availability of segregated post-consumer PET, demand for modular and locally maintainable defences, and a context in which the project is conceived as a controlled pilot or demonstration rather than as a definitive coastal-defence design. Any pilot should proceed only after hydraulic, durability, environmental-release, and economic validation are completed. The unit is not currently recommended for application in highly energetic or critical coastal sectors.

4.8. Limitations

The findings reported here must be read in light of the following limitations: (i) no laboratory-scale or field-scale validation dataset is available for the proposed unit, so the framework remains internally verified and empirically contextualised but unvalidated against physical or field data; (ii) the equivalent loading scheme idealises the impact as a triangular pulse with a discrete set of peak velocities (3, 5, 7 and 10 m/s) rather than a continuous spectrum, and does not capture irregular wave trains, oblique incidence, infragravity waves, or breaking-induced impulsive pressures; (iii) the CFD scheme uses a smooth-surface idealisation with roughness assessed analytically, a cross-sectional flow representation, and a RANS k–ε closure, and does not resolve flow within and between individual units, wave obliquity or alongshore variability, or pore-scale flow; (iv) the results represent an idealised unit/profile-scale assessment and do not capture full armour-layer interaction, including inter-unit interlocking, displacement of individual units, progressive armour-layer failure, toe stability, scour, and sediment transport; (v) long-term durability of the composite under marine processes (chloride ingress, sulphate attack, wetting–drying cycles, UV exposure, abrasion, fatigue, biofouling, PET–cement interface degradation) has not been characterised; (vi) microplastic release and leachate behaviour of the PET fraction have not been quantified for the specific composite; (vii) the LCA is preliminary, cradle-to-gate, and excludes installation, use, maintenance, and end-of-life modules; (viii) no whole-life-cost economic analysis is included; (ix) the interfacial bond–shear strength of the specific PET–concrete mix has not been experimentally characterised, so the equivalent-solid FEA idealisation may underestimate local failure risk (Section 2.3); and (x) the baseline slope-stability analysis uses adopted screening-level geotechnical parameters consistent with published regional ranges, not site-specific laboratory or in situ test results. The hydraulic indicators reported here are system/profile-level quantities, while the material and embodied-carbon indicators are unit-level estimates; a complete like-for-like comparison with rip-rap would require a functional unit defined per linear metre of protected coastline at an equivalent protection level. The absence of experimental or field validation limits the external transferability of the results, although it does not invalidate the internal comparative logic of the framework.

Given these limitations, the evidence level of this study is numerical and comparative; it is suitable for hypothesis generation and design screening of modular coastal-protection concepts based on recycled-PET valorisation, not for final engineering design. This explicit framing is intended to delimit the use of the reported figures and to guide the staged research path described in Section 4.9.

4.9. Future Research Roadmap

A staged research path is required to move from the present preliminary evaluation toward field implementation: (i) laboratory characterisation of the PET–concrete composite at varying dosages (5–20% PET), including compressive and flexural strength, water absorption, and microstructure; (ii) small-scale physical-model testing in a wave flume under regular and irregular wave trains, including oblique wave incidence, to screen run-up velocities, overtopping, and unit stability; (iii) prototype-scale fabrication and instrumented testing of the modular unit, including prototype-scale monitoring of inter-unit interaction and dynamic response, together with a coupled geotechnical assessment of the protected-slope factor of safety; (iv) marine-durability evaluation, including abrasion, sulphate attack, wetting–drying cycles, UV exposure, microplastic release, and leachate characterisation; (v) full cradle-to-grave LCA including transport, installation, service-life maintenance, and end-of-life modules; (vi) detailed whole-life-cost economic analysis covering material, precasting, logistics, installation, maintenance, and replacement costs; and (vii) controlled pilot deployment in a low-energy coastal sector with monitoring of hydraulic, structural, durability, and ecological indicators over multiple years. Stages (ii)–(iii) are required to convert the present screening-level results into experimentally validated performance figures.

5. Conclusions

This work presented a screening-level numerical assessment of a hollow modular unit fabricated with a recycled PET–concrete composite, evaluated through a parallel, one-way comparative FEA–CFD workflow, proposed for coastal slope protection and stabilisation in Chucuito, Callao, Peru.

Technical findings. Within the simulation assumptions, the hollow PET–concrete configuration suggests run-up velocity reductions of approximately 56% at $\theta = 60^\circ$ and 52% at $\theta = 53^\circ$ (an average of $\approx$54% across the two energetic configurations) relative to a rip-rap baseline under the conservative 10 m/s scenario. Under the site-referenced velocity scenarios (3, 5 and 7 m/s at $\theta = 53^\circ$, anchored to the maximum flow velocity of 5 m/s from the site-specific Delft3D inundation model [21]), the corresponding midpoint reductions were approximately 57% at 3 and 5 m/s and approximately 25% at 7 m/s, where the rip-rap and hollow-unit velocity ranges overlapped substantially; the maximum free-surface elevations of the hollow-unit configuration were 7.77, 9.36 and 10.98 m, respectively, and at 7 m/s, the free surface exceeded the 10.4 m crest, indicating a substantially reduced comparative advantage at the upper sensitivity case. In the conservative 10 m/s angle-comparison runs, the simulated free surface remained below the 10.4 m model crest at $\theta = 53^\circ$ and 45°, reaching approximately 10.28 m and 9.42 m, respectively; this observation is specific to those angle-comparison runs and does not apply to the 7 m/s velocity-sensitivity case at $\theta = 53^\circ$, where the simulated free surface reached approximately 10.98 m and exceeded the crest. These results are conditional on the smooth-surface CFD scheme with analytical roughness assessment and on the model geometry (defence height $H = 10.4$ m) and should not be read as an overtopping verification of the actual coastal defence. Under the adopted basal restraint, the FEA showed consistent comparative displacement and residual-energy trends across the tested configurations; these results provide a structural-response screening under a common boundary condition and do not independently test resistance to overturning or basal separation. The baseline limit-equilibrium analysis showed the unprotected slope to be marginal to unstable (static FS of 0.98–1.11 for the surficial silty sand; pseudo-static FS below or at the limit of the normative requirement for both bounding soils), confirming the geotechnical case for surface protection and stabilisation measures. The CFD output for the rip-rap baseline showed the same order of magnitude as indicative ranges from established empirical frameworks (≈3–6 m/s for plunging-wave conditions at the breaking depth, and free-surface elevations between the EurOtop estimates for the site's design wave heights), supporting its use as a comparative indicator only.

Environmental and circularity findings. The hollow geometry uses approximately 38% of the equivalent solid-block volume (≈62% material saving per functional unit), and the proposed unit valorises approximately 793 post-consumer 3 L PET bottles per unit (≈51 kg of PET, equivalent to ≈1015 bottles for lighter 50 g formats) at a 10% volumetric dosage. A simplified cradle-to-gate estimate with sensitivity analysis suggests a 42–58% embodied-CO_2 reduction (central case ≈ 50%) relative to the solid-concrete reference; this benefit is driven mainly by the hollow geometry, while the recycled-PET fraction contributes the plastic-waste valorisation co-benefit. Detailed quantitative figures and sensitivity ranges are reported in Sections 3.6 and 3.7 and depend on local supply-chain assumptions.

Limitations. The study is preliminary and numerical. It lacks experimental validation, uses an equivalent loading scheme rather than irregular waves, does not resolve flow within the armour layer, does not represent inter-unit interaction or scour, does not characterise durability or microplastic release of the composite under marine exposure, and includes neither a full cradle-to-grave LCA nor a whole-life-cost economic analysis. The reported figures should not be used as design criteria for site implementation.

Next validation stage. Required follow-up steps include laboratory characterisation of the composite, wave-channel testing under irregular wave conditions, prototype-scale fabrication and instrumented testing, marine-durability and microplastic-release assessment, full cradle-to-grave LCA, whole-life-cost economic analysis, and a controlled pilot deployment with multi-year monitoring.

This study combines recycled-PET valorisation, hollow modular geometry, comparative parallel FEA–CFD simulation, circularity indicators, and a sensitivity-tested embodied-CO_2 estimate in a vulnerable Latin-American coastal setting. The loading scenarios are anchored to the official site-specific inundation modelling for Chucuito [21], aligning the screening framework with the risk-management instruments in force for the study area. The framework is intended for early-stage screening and hypothesis generation, not for engineering design or direct implementation, and provides a defensible numerical baseline on which subsequent experimental and field studies can build. The proposal connects to specific Sustainable Development Goal targets: SDG 11.5 (reduction of losses caused by disasters, through coastal-resilience indicators), SDG 12.5 (substantial reduction of waste generation through recycling, through PET valorisation per functional unit), and SDG 13.1 (strengthening resilience and adaptive capacity to climate-related hazards, through low-carbon adaptation infrastructure). By indicating that within this case study, geometric design rather than material substitution alone drives the dominant share of the estimated embodied-carbon savings, the results point to a candidate design principle, prioritising void geometry over material substitution as a carbon-reduction lever, that warrants testing across other recycled-content modular coastal-defence concepts before it can be generalised.

Supplementary Materials: The following supporting information can be downloaded at: https://www.mdpi.com/article/10.3390/su18168201/s1, Table S1: Numerical-simulation parameters adopted for the FEA structural-response screening and the companion CFD analysis.

Author Contributions: Conceptualisation, T.R.V.V., M.C.C.F. and G.Y.T.; methodology, T.R.V.V., O.V.H., M.C.C.F. and G.Y.T.; software, T.R.V.V. and M.F.V.M.; validation, T.R.V.V., O.V.H., M.C.C.F., M.F.V.M. and J.C.G.A.; formal analysis, T.R.V.V., M.C.C.F., G.Y.T., A.D.M.H. and J.C.G.A.; investigation, T.R.V.V., O.V.H., M.C.C.F., G.Y.T., A.D.M.H. and J.C.G.A.; resources, M.C.C.F. and H.A.V.C.; data curation, T.R.V.V., M.F.V.M. and J.C.G.A.; writing–original draft preparation, T.R.V.V., M.C.C.F. and G.Y.T.; writing–review and editing, T.R.V.V., O.V.H., M.C.C.F., G.Y.T., M.F.V.M., D.N.H.A., A.D.M.H., H.A.V.C. and J.C.G.A.; visualisation, T.R.V.V., M.F.V.M. and J.C.G.A.; supervision, M.C.C.F. and H.A.V.C.; project administration, M.C.C.F. All authors have read and agreed to the published version of the manuscript.

Funding: This research received no external funding.

Institutional Review Board Statement: Not applicable.

Informed Consent Statement: Not applicable.

Data Availability Statement: The data supporting the findings of this study comprising the CFD outputs (run-up velocity ranges and water-surface elevation along the slope) for each configuration, the geometry files of the hollow PET–concrete unit (in STEP/IGES format), and the LCA central-case and sensitivity-analysis spreadsheets used to generate Tables 11 and 12 are available from the corresponding author upon reasonable request.

Acknowledgments: The authors thank the Directorate of Hydrography and Navigation (HIDRONAV) of the Peruvian Navy for the publicly available coastal-environment information used as a reference in the load definition. During the preparation of this manuscript, the author(s) used Claude Sonnet 4.5 (Anthropic) to support the implementation of the limit-equilibrium calculation scripts described in Section 2.5. The authors reviewed and edited the output and take full responsibility for the content of this publication.

Conflicts of Interest: The authors declare no conflicts of interest.

Abbreviations

The following abbreviations are used in this manuscript:

PET	Polyethylene terephthalate
FEA	Finite-element analysis
NbS	Nature-based solutions
EbA	Ecosystem-based adaptation
LCA	Life-cycle assessment
SDG	Sustainable development goal
HIDRONAV	Directorate of Hydrography and Navigation (Peru)
CFD	Computational fluid dynamics
RANS	Reynolds-averaged Navier–Stokes
VOF	Volume of fluid
GWP	Global warming potential
FS	Factor of safety

References

1. Intergovernmental Panel on Climate Change (IPCC). *Climate Change 2023: Synthesis Report. Contribution of Working Groups I, II and III to the Sixth Assessment Report of the Intergovernmental Panel on Climate Change*; Core Writing Team, Lee, H., Romero, J., Eds.; IPCC: Geneva, Switzerland, 2023. [CrossRef]
2. Jigena-Antelo, B.; Estrada-Ludeña, C.; Howden, S.; Rey, W.; Paz-Acosta, J.; Lopez-García, P.; Salazar-Rodriguez, E.; Endrina, N.; Muñoz-Pérez, J.J. Evidence of sea level rise at the Peruvian coast (1942–2019). *Sci. Total Environ.* **2023**, *859*, 160082. [CrossRef] [PubMed]
3. Organisation for Economic Co-operation and Development (OECD). *Global Plastics Outlook: Policy Scenarios to 2060*; OECD Publishing: Paris, France, 2022. [CrossRef]
4. Cottom, J.W.; Cook, E.; Velis, C.A. A local-to-global emissions inventory of macroplastic pollution. *Nature* **2024**, *633*, 101–108. [CrossRef] [PubMed]
5. Borrelle, S.B.; Ringma, J.; Law, K.L.; Monnahan, C.C.; Lebreton, L.; McGivern, A.; Murphy, E.; Jambeck, J.; Leonard, G.H.; Hilleary, M.A.; et al. Predicted growth in plastic waste exceeds efforts to mitigate plastic pollution. *Science* **2020**, *369*, 1515–1518. [CrossRef] [PubMed]

6. Ministerio del Ambiente del Perú (MINAM). *Informe Anual de Residuos Sólidos Municipales y No Municipales en el Perú 2023*; MINAM: Lima, Peru, 2024.
7. Ellen MacArthur Foundation. *Completing the Picture: How the Circular Economy Tackles Climate Change*; Ellen MacArthur Foundation: Cowes, UK, 2019.
8. *ISO 59004:2024*; Circular Economy—Vocabulary, Principles and Guidance for Implementation. International Organization for Standardization (ISO): Geneva, Switzerland, 2024.
9. Sharma, R.; Bansal, P.P. Use of different forms of waste plastic in concrete–A review. *J. Clean. Prod.* **2016**, *112*, 473–482. [CrossRef]
10. Saikia, N.; de Brito, J. Use of plastic waste as aggregate in cement mortar and concrete preparation: A review. *Constr. Build. Mater.* **2012**, *34*, 385–401. [CrossRef]
11. Akçaözoğlu, S.; Atiş, C.D.; Akçaözoğlu, K. An investigation on the use of shredded waste PET bottles as aggregate in lightweight concrete. *Waste Manag.* **2010**, *30*, 285–290. [CrossRef] [PubMed]
12. Kim, Y.C. (Ed.) *Design of Coastal Structures and Sea Defenses*; World Scientific: Singapore, 2014.
13. CIRIA; CUR; CETMEF. *The Rock Manual: The Use of Rock in Hydraulic Engineering*, 2nd ed.; CIRIA C683; CIRIA: London, UK, 2007.
14. van der Meer, J.W.; Pilarczyk, K.W. *Stability of Breakwater Armour Layers: Deterministic and Probabilistic Design*; Delft Hydraulics Communication, No. 378; Delft Hydraulics Laboratory: Delft, The Netherlands, 1987.
15. Bruce, T.; van der Meer, J.W.; Franco, L.; Pearson, J.M. Overtopping performance of different armour units for rubble mound breakwaters. *Coast. Eng.* **2009**, *56*, 166–179. [CrossRef]
16. Burcharth, H.F.; Hughes, S.A. Types and functions of coastal structures. In *Coastal Engineering Manual, Part VI, Chapter VI-2*; USACE: Washington, DC, USA, 2011.
17. Khan, M.S.; Nobahar, M.; Ivoke, J. Numerical Investigation of Slope Stabilization Using Recycled Plastic Pins in Yazoo Clay. *Infrastructures* **2021**, *6*, 47. [CrossRef]
18. Le Roux, J.P.; Tavares Correa, C.; Alayza, F. Sedimentology of the Rímac–Chillón alluvial fan at Lima, Peru, as related to Plio-Pleistocene sea-level changes, glacial cycles and tectonics. *J. S. Am. Earth Sci.* **2000**, *13*, 499–510. [CrossRef]
19. Dirección de Hidrografía y Navegación (HIDRONAV). *Boletín de Oleajes Anómalos para el Litoral Peruano*; Marina de Guerra del Perú: Callao, Peru, 2024.
20. Gravina, R.J.; Xie, T.; Bennett, B.; Visintin, P. HDPE and PET as aggregate replacement in concrete: Life-cycle assessment, material development and a case study. *J. Build. Eng.* **2021**, *44*, 103329. [CrossRef]
21. Gobierno Regional del Callao (GORE CALLAO). *Informe de Evaluación del Riesgo por Oleajes Anómalos en la Urb. Chucuito, Distrito del Callao, Provincia Constitucional del Callao, Departamento de Lima*; GORE CALLAO: Callao, Peru, 2024. Available online: https://sigrid.cenepred.gob.pe/sigridv3/documento/18352 (accessed on 25 May 2026).
22. *NTP 400.012:2013*; Agregados. Análisis Granulométrico del Agregado fino, Grueso y Global. Instituto Nacional de Calidad (INACAL): Lima, Peru, 2013.
23. Ochi, T.; Okubo, S.; Fukui, K. Development of recycled PET fibre and its application as concrete-reinforcing fibre. *Cem. Concr. Compos.* **2007**, *29*, 448–455. [CrossRef]
24. Sigrüner, M.; Hüsken, G.; Pirskawetz, S.; Herz, J.; Muscat, D.; Strübbe, N. Pull-out behavior of polymer fibers in concrete. *J. Polym. Sci.* **2023**, *61*, 2708–2720. [CrossRef]
25. Villacorta, S.P.; Evans, K.G.; De Torres, T.J.; Llorente, M.; Prendes, N. Geomorphological evolution of the Rimac River's alluvial fan, Lima, Peru. *Geosci. J.* **2019**, *23*, 409–424. [CrossRef]
26. Alva Hurtado, J.E.; Meneses Loja, J.; Martínez Del Rosario, J.; Huamán Egoávil, C.E. Avances en la Microzonificación Sísmica de Lima, Perú. In Proceedings of the Fourth International Conference on Seismic Zonation, Stanford, CA, USA, 26–29 August 1991.
27. Huamán, C. Microzonificación Sísmica de La Punta y El Callao. Bachelor's Thesis, Facultad de Ingeniería Civil, Universidad Nacional de Ingeniería, Lima, Peru, 1991.
28. CISMID-FIC-UNI. *Estudio de Microzonificación Sísmica y Análisis de Riesgo en Zonas de Estudio Ubicadas en el Área Urbana del Distrito del Callao (Cercado del Callao)*; Producto 03, Tomo III: Estimación del Riesgo; SIGRID/CENEPRED library, document 14511; CISMID-FIC-UNI: Lima, Peru, 2020.
29. Bishop, A.W. The use of the slip circle in the stability analysis of slopes. *Géotechnique* **1955**, *5*, 7–17. [CrossRef]
30. Ministerio de Vivienda, Construcción y Saneamiento (Perú). *Norma Técnica E.030 Diseño Sismorresistente*; Reglamento Nacional de Edificaciones, RM N.° 355-2018-VIVIENDA; Ministerio de Vivienda, Construcción y Saneamiento (Perú): Lima, Peru, 2018.
31. Ministerio de Vivienda, Construcción y Saneamiento (Perú). *Norma CE.020 Estabilización de Suelos y Taludes*; Reglamento Nacional de Edificaciones, D.S. N.° 017-2012-VIVIENDA; Ministerio de Vivienda, Construcción y Saneamiento (Perú): Lima, Peru, 2012.
32. *Engineer Manual EM 1110-2-1100*; Coastal Engineering Manual (CEM). U.S. Army Corps of Engineers (USACE): Washington, DC, USA, 2002.
33. van der Meer, J.W. Stability of breakwater armour layers—Design formulae. *Coast. Eng.* **1987**, *11*, 219–239. [CrossRef]

34. Van der Meer, J.W.; Allsop, N.W.H.; Bruce, T.; De Rouck, J.; Kortenhaus, A.; Pullen, T.; Schüttrumpf, H.; Troch, P.; Zanuttigh, B. *EurOtop: Manual on Wave Overtopping of Sea Defences and Related Structures—An Overtopping Manual Largely Based on European Research, but for Worldwide Application*, 2nd ed.; 2018. Available online: https://www.overtopping-manual.com (accessed on 2 March 2026).
35. Chopra, A.K. *Dynamics of Structures: Theory and Applications to Earthquake Engineering*, 5th ed.; In SI Units; Pearson: Hoboken, NJ, USA, 2019.
36. Prasetyo, H.; Budiana, E.P.; Tjahjana, D.D.D.P.; Hadi, S. The Simulation Study of Horizontal Axis Water Turbine Using Flow Simulation Solidworks Application. *IOP Conf. Ser. Mater. Sci. Eng.* **2018**, *308*, 012022. [CrossRef]
37. Prabhu, L.; Krishnamoorthi, S.; Gokul, P.; Sushan, N.; Hisham Harshed, P.H.; Jose, A. Aerodynamics analysis of the car using Solidworks flow simulation with rear spoiler using CFD. *IOP Conf. Ser. Mater. Sci. Eng.* **2020**, *993*, 012002. [CrossRef]
38. Vieira, F.; Taveira-Pinto, F.; Rosa-Santos, P. Single-layer cube armoured breakwaters: Critical review and technical challenges. *Ocean Eng.* **2020**, *216*, 108042. [CrossRef]
39. Bakker, P.; Ruwiel, T.; van de Koppel, M.; Yang, Z.Q.; Donnelly, J.A. Wave Overtopping Reduction by Modular Concrete Armour Units. In Proceedings of the 37th International Conference on Coastal Engineering, Sydney, Australia, 4–9 December 2022.
40. Eldrup, M.R.; Andersen, T.L.; Burcharth, H.F. Stability of rubble mound breakwaters—A study of the notional permeability factor, based on physical model tests. *Water* **2019**, *11*, 934. [CrossRef]
41. Hibbeler, R.C. *Engineering Mechanics: Dynamics*, 14th ed.; Pearson: Hoboken, NJ, USA, 2016.
42. Jiménez, L.F.; Domínguez, J.A.; Vega-Azamar, R.E. Carbon footprint of recycled aggregate concrete. *Adv. Civ. Eng.* **2018**, *2018*, 7949741. [CrossRef]
43. Hottle, T.; Hawkins, T.R.; Chiquelin, C.; Lange, B.; Young, B.; Sun, P.; Elgowainy, A.; Wang, M. Environmental life-cycle assessment of concrete produced in the United States. *J. Clean. Prod.* **2022**, *363*, 131834. [CrossRef]
44. Lopes, L.; Dauari, H.; Mendonça, P.; Almeida, M. Marine plastic waste in construction: A systematic review of applications in the built environment. *Polymers* **2025**, *17*, 1729. [CrossRef] [PubMed]
45. European Commission. *A New Circular Economy Action Plan: For a Cleaner and More Competitive Europe*; COM(2020) 98 final; European Commission: Brussels, Belgium, 2020. Available online: https://eur-lex.europa.eu/legal-content/EN/TXT/?uri=COM:2020:98:FIN (accessed on 2 March 2026).
46. Poder Ejecutivo del Perú. *Decreto Legislativo N° 1278 que aprueba la Ley de Gestión Integral de Residuos Sólidos*; Diario Oficial El Peruano: Lima, Peru, 2016. Available online: https://www.minam.gob.pe/disposiciones/decreto-legislativo-n-1278/ (accessed on 2 March 2026).
47. Congreso de la República del Perú. *Ley N° 30884 que Regula el Plástico de un Solo Uso y los Recipientes o Envases Descartables*; Diario Oficial El Peruano: Lima, Peru, 2018. Available online: https://www.gob.pe/institucion/congreso-de-la-republica/normas-legales/227298-30884 (accessed on 2 March 2026).
48. Abubakar, L.; Yeasmin, N.; Bhattacharjee, A. Waste polyethylene terephthalate (PET) as a partial replacement of aggregates in sustainable concrete. *Constr. Mater.* **2024**, *4*, 738–747. [CrossRef]
49. Kazemi, M.; Faisal Kabir, S.; Fini, E.H. State of the art in recycling waste thermoplastics and thermosets and their applications in construction. *Resour. Conserv. Recycl.* **2021**, *174*, 105776. [CrossRef]
50. Sau, D.; Shiuly, A.; Hazra, T. Utilization of plastic waste as replacement of natural aggregates in sustainable concrete: Effects on mechanical and durability properties. *Int. J. Environ. Sci. Technol.* **2024**, *21*, 2085–2120. [CrossRef] [PubMed]
51. Saxena, R.; Siddique, S.; Gupta, T.; Sharma, R.K.; Chaudhary, S. Impact resistance and energy absorption capacity of concrete containing plastic waste. *Constr. Build. Mater.* **2018**, *176*, 415–421. [CrossRef]
52. Silva, D.A.; Betioli, A.M.; Gleize, P.J.P.; Roman, H.R.; Gómez, L.A.; Ribeiro, J.L.D. Degradation of recycled PET fibers in Portland cement-based materials. *Cem. Concr. Res.* **2005**, *35*, 1741–1746. [CrossRef]